



LAWRENCE
LIVERMORE
NATIONAL
LABORATORY

From microjoules to megajoules and kilobars to gigabars: probing matter at extreme states of deformation*

B. Remington, R. Rudd, J. Wark

June 11, 2015

APS-DPP 2014

New Orleans, LA, United States

October 27, 2014 through October 31, 2014

Disclaimer

This document was prepared as an account of work sponsored by an agency of the United States government. Neither the United States government nor Lawrence Livermore National Security, LLC, nor any of their employees makes any warranty, expressed or implied, or assumes any legal liability or responsibility for the accuracy, completeness, or usefulness of any information, apparatus, product, or process disclosed, or represents that its use would not infringe privately owned rights. Reference herein to any specific commercial product, process, or service by trade name, trademark, manufacturer, or otherwise does not necessarily constitute or imply its endorsement, recommendation, or favoring by the United States government or Lawrence Livermore National Security, LLC. The views and opinions of authors expressed herein do not necessarily state or reflect those of the United States government or Lawrence Livermore National Security, LLC, and shall not be used for advertising or product endorsement purposes.

From microjoules to megajoules and kilobars to gigabars:
probing matter at extreme states of deformation*

Bruce A. Remington and Robert E. Rudd
Lawrence Livermore National Laboratory, Livermore, CA 94550 USA

Justin S. Wark
Department of Physics, Clarendon Laboratory, University of Oxford, Oxford, , OX1 3PU UK

Abstract

Over the past 3 decades there has been an exponential increase in work done in the newly emerging field of matter at extreme states of deformation and compression. This accelerating progress is due to the confluence of new experimental facilities, experimental techniques, theory, and simulations. Regimes of science hitherto thought out of reach in terrestrial settings are now being accessed routinely. High-power lasers and pulsed power facilities are accessing high-pressure macroscopic states of matter, and next-generation light sources are probing the quantum response of matter at the atomistic level. Combined, this gives experimental access to the properties and dynamics of matter from femtoseconds to microseconds in time scale and from kilobars to gigabars in pressure. There are a multitude of new regimes of science that are now accessible in laboratory settings. Examples include planetary formation dynamics, asteroid and meteor impact dynamics, space hardware response to hypervelocity dust and debris impacts, nuclear reactor component response to prolonged exposure to radiation damage, advanced research into light weight armor, and capsule dynamics in inertial confinement fusion (ICF) research. We will review highlights and advances in this rapidly developing area of science and research.

I. Introduction

There is an enduring interest in understanding the properties of matter at high pressures and compressions, driven partly by a desire to understand the structures and properties of planetary interiors, and their formation dynamics. An obvious example is our interest to understand the interior structure of the Earth, as illustrated by the phase diagram for iron in Fig. 1a. Understanding the phase and melt curve of iron at high pressure advances our understanding of the Earth,¹⁻³ and Earth-like exoplanets, such as the so-called “Super-Earths”.⁴⁻¹⁰ In another arena, motivated by the requirements of the inertial confinement fusion (ICF) program,¹¹⁻¹⁶ material properties, such as equations of state, opacities, reflectivities, and conductivities, have become important to know quantitatively over a very wide range extending from near ambient to very high pressures (kbars to gigabars). Furthermore, the requirements of the ICF ignition program drive the need to understand material properties to pressures as high as 100 Gbar (10^4 TPa) and compressions, ρ/ρ_0 , of a few up to as high as ~ 1000 . This has opened up an experimental branch of science studying matter under conditions relevant to the interiors of planets and stars. Also, a new focus area of laboratory astrophysics at high energy density (HED) conditions has emerged.¹⁷⁻¹⁹ The setting for these experiments are typically high-power lasers and magnetic pinch facilities. The energies of these drivers range from microjoules (in university laboratories) to megajoules (at the national laboratories). We review here the field of material science and material dynamics over these ranges of pressures and compressions. This work is distinct from, but complementary to, the work done on diamond anvil cells (DAC) to study material properties. The DAC experiments can reach high pressures, up to ~ 600 GPa, but under quasi-static, isothermal conditions.²⁰ The work reviewed here is all dynamic (time resolved) and adiabatic, in the sense that heat created during compression or release largely remains within the samples

studied. A remarkable result of this “extreme materials science” is the realization that one of the most useful theoretical and simulation tools for exploring these unique regimes of extreme pressures and rates of compression, namely, molecular dynamics (MD) simulations, occur over comparable spatial and temporal scales as the HED experiments.²¹ This confluence allows reasonably direct comparisons between experiments and the quantum mechanically based interatomic potentials that reside at the core of classical MD simulations.

Significant experimental and technological challenges have been overcome over the past three decades to allow such extreme HED states of matter to be probed. On the drive side, there have been tremendous advances in getting precise drives from laser pulse-shaping, current pulse shaping at magnetic pinch facilities, and target based pulse shaping that allow a sequence of staged compression waves or ramp waves to compress matter along a near-isentrope to extraordinarily high pressures. Advanced diagnostic techniques continue to be developed at a rapid pace. VISAR diagnostics allow the drive and compression waves to be diagnosed with precision. In-flight, time resolved x-ray radiography allows the compression of matter to be measured directly. X-ray Thomson scattering allows the plasma electron density, temperature, ion density, and velocity to be measured, thus characterizing the environment. To probe samples that are compressed to high pressure in the solid state, time resolved x-ray diffraction (Bragg, Laue, and powder) have been developed to probe the sample at the lattice level. Time resolved EXAFS diagnostics allow the sample phase, compression, and temperature to be measured at the atomic level. The large laser and magnetic pinch facilities allow matter to be prepared at very high pressure and density conditions, matching the conditions at the centers of the planets. And 4th generation light sources allow matter to be probed with exquisite signal to noise, accuracy, and time resolution. Each of these techniques will be described and illustrated in the sections below, in the context of experiments that have been carried out over the past 30 years on a wide variety of HED experimental facilities.

This paper is organized as follows. In Sec. II, we start by giving an example of how the field of dynamic properties of materials started in the 1960s and 1970s. We describe a widely cited wave profile measurement of shock loaded iron based on powder gun driven plate impact in which the α to ϵ (bcc to hcp) phase transition in iron was deduced. We also include in this section examples of modern laser and Z-pinch driven, ramp compression experiments on iron to measure wave shapes, and determine the α - ϵ phase transition stress as a function of strain rate. Then we describe in Sec. III the first time-resolved diffraction experiments, carried out in shocked single crystal Si on ICF class pulsed lasers. In Sec. IV, we review a series of high-rate, high-pressure experiments on copper, a face-centered cubic (fcc) metal. Then in Sec. V we describe time resolved diffraction experiments on shocked iron, in which the α to ϵ (bcc to hcp) phase transition was observed for the first time at the lattice level. Section VI presents high pressure experiments in MgO, motivated by planetary science research. First, experiments using a decaying shock technique are described that inferred the liquid to solid transition and the B2 to B1 solid-solid phase transitions, using time resolved velocimetry and optical pyrometry. Then we describe results of diffraction experiments on ramp loaded MgO at very high pressures, to demonstrate the B1-to-B2 solid-solid phase transition at the lattice level. We describe in Sec. VII the first dynamic extended x-ray absorption fine structure (EXAFS) measurements on shocked vanadium to deduce temperature and density behind the shock, and shocked iron to infer the phase. In Section VIII, we describe EXAFS measurements on off-Hugoniot iron loaded to peak pressures approaching 600 GPa (6 Mbar). Then Sec. IX presents a series of high-pressure experiments in Ta, integrated and at the lattice level, including a discussion of a Ta multiscale strength model. Sec. X presents results of experiments to measure the entropy on the Hugoniot in shocked SiO₂ and to determine its vaporization curve on release. We also describe a high pressure decaying shock experiment in SiO₂ which inferred the melt curve for fused silica, quartz, and stishovite. In Sec. XI, results

describing decaying shock experiments at high pressure in diamond (carbon) starting from a peak shock strength of ~ 2 TPa). We also describe ramp compression experiments in carbon to 5 TPa (50 Mbar) peak pressures, with comparisons to a number of theoretical calculations. We describe the development of experiments to study the properties of matter at pressures approaching 100 TPa (1 Gbar) in Sec. XII. We also describe the recent development of time resolved x-ray Thomson scattering (XRTS) diagnostic technique to be able to probe the temperature, density, and at some level, structure of matter at extreme conditions of density and temperature. We finish with a short conclusion in Sec. XIII.

II. Compression Wave Profile Experiments in Iron

Reaching the regimes required to study the properties of matter at Earth interior conditions requires high pressures and high densities, as illustrated in Fig. 1a.³ To study iron at Earth core conditions will requires reaching pressures of 300-400 GPa at temperatures of 5000-6000 K, which is near to but just below the melt temperature at these pressures. A promising experimental approach for reaching these conditions is an initial strong shock followed by ramp compression to the required pressures and temperatures.³ We first describe below an early experiment to shock iron using plate impact experiments, followed by more recent work on developing the required ramp compression part of the loading to reach the highest pressures without melting the iron.

The study of the dynamic behavior of matter was pursued in the 1970s with experiments using plate impact techniques to produce planar shocks in samples and measuring the resulting free-surface velocities with Velocity Interferometer System for Any Reflector (VISAR) diagnostics. The free-surface velocity measurements in shocked iron provided the first suggestion of a shock driven polymorphic phase transition in iron at a shock strength of around 13 GPa, which was interpreted as the α - ϵ (bcc-hcp) transition. An example of such a free surface velocity measurement for shocked iron using a powder gun to generate a plate impact is shown in Fig 1b, for a peak shock stress of 23.7 GPa.²² The structure in this velocity profile corresponds to the elastic precursor (E), the first plastic wave (P1) corresponding to the onset of the transition from the α to the ϵ phase, the second plastic wave (P2) corresponding to “the wave which carries the material from the α phase to the peak stress level in the ϵ phase”, and the phase interface reflection (PIR) wave, which is an artifact of reflecting off a free back surface.²² The measurement, and its predecessor by Bancroft [Bancroft 1956], helped kick off the field of dynamic properties of matter.²³

More recent generations of experiments have focused on developing off-Hugoniot ramp wave loading techniques, to be able to study the properties of matter in the solid state at much higher pressures. Figure 1c shows a free-surface velocity versus time measurement from such a ramp wave experiment done on iron²⁴ at the Sandia Z-machine.²⁵ The velocity plateau at $u_{fs} \sim 0.75$ km/s is attributed to the onset of the α - ϵ phase transformation in iron. An interesting observation, shown in the inset, is that the α - ϵ phase transition velocity plateau decreases with time, as a result of the time dependence of the transition, that is, phase transition kinetics. When more time is available for the phase transition to occur, its onset is observed at a slightly lower uniaxial loading stress. This point becomes important when looking for phase transitions in high rate loading environments, where high pressure conditions in the sample can only be held for short durations of time.

To more fully explore the effects of loading rates on wave profile evolution in ramp compressed iron, a compendium of results is shown in Fig. 1d,²⁴ from experiments done on the Janus²⁶ and Omega²⁷ lasers, a micro-joule laser at LLNL,²⁸ and the Z pulsed power facility. What is plotted is

the uniaxial loading stress required to initiate the α - ϵ phase transition in iron, as a function of the strain rate associated with the transition. This figure is particularly noteworthy, because it shows that the higher the loading rate, the higher the observed α - ϵ phase transition stress. Above a strain rate of $\sim 10^6 \text{ s}^{-1}$, this effect is particularly significant. The inset of Fig. 1d shows a similar effect, only for the peak elastic precursor stress, marking the onset of plastic flow in iron. The sudden increase of elastic – plastic transition stress at strain-rates $> \sim 10^6 \text{ s}^{-1}$ is suggested to result from a transition from thermal activation to a phonon drag regime of plastic flow.²⁴

Sound speeds are a fundamental quantity that determine how rapidly information can be transmitted within bulk material under subsonic conditions. Experimentally determining sound speeds for high pressure, planetary interior conditions is a difficult task. Over the last 5 years, Sakaiya et al. have developed a technique to experimentally determine sound speeds in metals at pressures approaching 10 Mbar on the Gekko-XII laser facility.²⁶ The technique is based on side-on x-ray radiography, and illustrated in the two insets of Fig. 1e.^{26,27} By comparing shock breakout time on the back surface of a planar foil, to the onset of acceleration of the front surface of the foil, the velocity of the rarefaction from the rear surface at shock release to the front, driven surface), can be determined. This velocity is equivalent to the sound speed at pressure. Figure 1e shows measured sound speeds as a function of sample pressure in iron up to nearly 10 Mbar from the Gekko-XII experiments, and overplots these with values from lower pressure experiments using more traditional techniques.²⁸

There is a very wide interest worldwide currently to understand as much as possible about the newly discovered exoplanets, that is, planets and planetary systems discovered outside of our solar system. One intriguing category of exoplanets are the so-called “Super-Earths”, which correspond to terrestrial planets like earth, but at 5-10 times the mass. Understanding the properties of the interiors of such planets, such as whether conditions would support formation of a planetary magnetic field, address aspects of whether such planets could harbor life as we know it. Astronomical observations cannot tell us such details, but modern laboratory experiments on HED laser facilities, such as the LIL facility in France, can both prepare matter and probe it in states relevant to the interiors of the Super-Earths. For example, the experiment by Amadou et al.^{24c} used the LIL laser in France to generate a long ($\sim 20 \text{ ns}$), highly shaped ramp compression, with laser power contrast ratio (peak/foot) of ~ 20 or more, as shown by the inset of Fig. 1f. Experiments were specifically designed to probe iron (Fe) using this drive, at pressures and temperatures in the Fe spanning up to 7 Mbar and 8000 K, as shown in Fig. 1f. The measurements were performed with simultaneous VISAR and SOP diagnostics looking at the conditions at the Fe – Sapphire window interface, where sapphire was the transparent window on the back side of the Fe sample. [See Ref. 28 for more details.]

III. Diffraction on Shocked Silicon

The first time-resolved, dynamic diffraction experiments using an ICF class laser, the Janus laser at LLNL, launched a $\sim 7 \text{ GPa}$ (70 kbar) shock through a $250 \mu\text{m}$ thick single crystal sample of [111] Si, as shown in Fig. 2. [^{29,32}] The experimental configuration is shown in Fig. 2a, and time resolved diffraction data showing a shock compressed lattice is given in Fig. 2b. The drive was generated by direct illumination of a 1 ns FWHM Gaussian pulse of $1 \mu\text{m}$ light at an intensity of $\sim 4 \times 10^9 \text{ W/cm}^2$. A second synchronized but delayed laser beam, 10 J at a wavelength of $0.53 \mu\text{m}$ and a 100 ps Gaussian pulse shape, generated a burst of Ca He- α x-rays at $\sim 3.9 \text{ keV}$ to record a time-resolved Bragg diffraction signal, which measured the lattice response to the shock in Si. As the diffraction signal was recorded from a single plane, the data were not sufficient to

differentiate whether the observations corresponded to a one dimensional (1D) elastic compression or a three dimensional (3D) relaxed plastic compression. Nevertheless, the ability to do time-resolved, nanosecond scale, microscopic, lattice level measurements of the crystal response to a “strong” shock (in the sense of a stress of order tens of kbar) had now been experimentally demonstrated.

A decade later on the Nova laser, an experiment using an x-ray drive acquired a more substantial set of data reaching higher shock pressures, as shown in Fig. 3.³³ The experimental configuration used a hollow cylindrical Au radiation cavity (“hohlraum”), as shown in Fig. 3a, to convert the 351 nm drive laser into a Planckian radiation drive of radiation temperatures $T_r \sim 20\text{-}60$ eV. This radiation was used to launch shocks of 19, 26, and 60 GPa strength along the [400] direction of the single crystal Si. The diffraction from the (400) lattice plane in the direction of the shock velocity was streaked in time, to give continuous time coverage, as shown in Fig. 3b. The time-averaged diffraction profile for each shock from the (400) lattice planes are shown in Fig. 3c. The stronger the shock, the smaller the normalized lattice spacing, d/d_0 , where d and d_0 correspond to the lattice spacing for the shocked and unshocked lattice planes. The corresponding patterns for diffraction from the (040) lattice planes, transverse to the direction of shock motion, are shown in Fig. 3d. These transverse lattice planes showed no observable lattice compression, even once the compression wave had reached the rear surface of the sample. This was interpreted as demonstrating that on the nanosecond time scales of the experiment, the shocked single crystal Si did not have time to evolve plastically to a 3D relaxed state; the observed diffraction was consistent with a 1D elastic compression, with the (040) lattice spacing transverse to the [400] shock direction remaining unchanged over the ~ 2 ns of the experiment. The sharpness of the (040) diffraction peaks shown in Fig. 3d confirmed the low density of dislocations and other shock-induced lattice defects, at least within the leading region of the compression wave profile. Recent MD simulations³⁴ suggest that following the initial elastic wave the Si may have undergone a transition to a mixed phase (which, owing to the lattice constant of the new phase relieves the large shear stresses without the need for conventional plastic flow). This forms crystallites sufficiently small that the associated diffraction peaks were too broad to have been observed in the experimental geometry. That said, those MD simulations still do not seem to be able to predict correctly many aspects of the experimental results. Remarkably, after many years of study, full knowledge of the nanosecond response to compression of one of the purest, defect-free, crystals known remains elusive.

IV. Diffraction on Shocked Copper

In the same work by Loveridge-Smith,³³ a 2 μm thick single crystal Cu sample was shocked at a strength of ~ 18 GPa along the [200] direction, and Bragg diffraction signals were recorded from the (200) and (020) face-centered cubic (fcc) lattice planes (not shown). The shock was generated by direct illumination (“direct-drive”) of the laser on the single crystal Cu sample on the Omega laser. In these shocked Cu experiments, the lattice promptly relaxed plastically such that the lattice spacing in the transverse (020) direction and the shocked axial (200) direction were nearly the same. Estimates based on Orowan’s equation,

$$d\varepsilon_p/dt \sim \rho_{\text{disloc}} v_{\text{disloc}} b, \quad (1)$$

where ε_p , ρ_{disloc} , v_{disloc} , and b correspond to plastic strain rate, mobile dislocation density, average dislocation velocity, and Burger’s vector, suggest that the dislocation density behind the shock was high, $\rho_{\text{disloc}} \sim 10^{11}\text{-}10^{12} \text{ cm}^{-2}$, and that these dislocations were sufficiently mobile so as to relieve the shear stress within a few hundred picoseconds. Such a response is consistent with the

lower Peierls stress for the metallic fcc Cu than for the covalently-bonded diamond-cubic Si. However, the time resolution of the shocked Cu experiment performed on the Omega laser was insufficient to actually resolve the relaxation time.

Our understanding of the response of a simple fcc metal such as Cu has been greatly enhanced by the development of large scale molecular dynamics (MD) simulations, which now can encompass the time (nanosecond) and length (micron) scales of the laser-based experiments. The initial MD simulations,³⁵ constrained to only a few tens of picoseconds, demonstrated the rapid generation of defects in shocked fcc metals, but did not capture the full 1D to 3D relaxation seen in the experiments discussed above, as plasticity occurs via the subsequent motion of these dislocations.³⁶ With rapid developments in computing power, larger and longer simulations of shocked single crystal [100] Cu were carried out,³⁷ as shown in Figs. 4a using the embedded atom model (EAM) interatomic potential by Mishin.³⁸ These simulations enabled the 1D-3D relaxation time scale, τ_{1D-3D} , to be studied numerically as a function of shock front rise time (0 ps vs. 50 ps). The shock strength was 35 GPa, whereas the homogeneous (dislocation) nucleation threshold was observed in the simulations to be ~ 30 GPa. One of the main conclusions of this MD simulation study was that the plastic relaxation time behind the shock, τ_{1D-3D} , was of order ~ 30 ps., as shown in Fig. 4b giving the time evolution (relaxation) of the shear stress behind the shock. Above the homogenous nucleation threshold, for the steep shock front (0 ps rise time), the dislocation density behind the shock was high, $\sim 3 \times 10^{13} \text{ cm}^{-2}$. In simulations with pre-existing sources (dislocation loops), and a ~ 50 ps rise time on the shock front, the final dislocation density was about a factor of 3 lower at $\sim 1 \times 10^{13} \text{ cm}^{-2}$. The relaxation times were similar, however, suggesting a higher average dislocation velocity for the ramped shock case. This also led to the prediction that, even in the case of real metals with initial defects, elastic response right up to the ultimate theoretical uniaxial compressive strength of the material should be attainable on timescales of tens of picoseconds.

The ground-breaking diffraction experiments described above were performed with quasi-monochromatic x-ray sources emitted from plasmas created by high-intensity optical pulses synchronous to the pulse launching the shock in the sample. The duration of the probe x-ray sources (“backlighters”) were limited mainly by the duration of the optical laser pulse, which in most cases ranged from 100 ps to 1 ns. However, with the advent of Free Electron Lasers such as the Linac Coherent Light Source (LCLS) at SLAC, it is now possible to make shock diffraction measurements with better than 100-fsec time resolution – i.e. shorter than the period of the fastest phonon in the system. Furthermore, the bandwidth of the x-rays is of order a few times 10^{-3} , and can be reduced further by monochromating crystals. A recent experiment was performed using the Coherent X-ray Imaging Instrument (CXI) at LCLS to study time-resolved powder diffraction from shocked polycrystalline Cu, for a shock strength of ~ 70 GPa.³⁹ These polycrystalline samples had an average grain size of ~ 400 nm, and were highly textured, with a dominant $\langle 111 \rangle$ orientation normal to the target surface, which is also the direction of the shock compression wave.. The experimental setup for this experiment is shown in Fig. 4c, and simulations that reproduce the analyzed experimental results are shown in 20 ps steps in Fig. 4d. The time evolution from a 1D elastically compressed lattice to a more 3D relaxed lattice spacing is evident. Further calculations shown in Fig. 4e more clearly quantify the onset of plasticity, with curves of normal elastic strain, transverse plastic strain, and transverse elastic strain vs. time. The time lag between the elastic compression and the onset of plastic response is ~ 50 -70 ps, and occurs only when the normal elastic strain in the [111] direction has reached $\sim 18\%$. This ~ 50 ps 1D-3D relaxation time scale is reasonably close to the MD predictions of ~ 30 ps from MD simulations, albeit for a 35 GPa shock in single crystal Cu sample. This same analysis of the experimental data gives a shear stress (strength) of ~ 10 -20 GPa. In Fig. 4f, the results of a set of MD simulations are shown, giving stress-strain curves for compression of Cu along the [123],

[110], [111] and [001] directions at a temperature of 300 K and strain rate of 10^8 s^{-1} .⁴⁰ The strain threshold for dislocation nucleation (onset of plasticity) is indicated with arrows. For the [111] compression, an elastic strain of 16-20% is predicted before the transition to a plastically relaxed state, with a peak shear stress of $\tau_{\text{shear}} \sim 15\text{-}20 \text{ GPa}$, in good agreement with the LCLS experiment of shocked Cu (Fig. 4e). What is remarkable about these results is that the temporal and spatial scales of the various MD simulations and the LCLS experiment match, and the predicted relaxation times are in reasonable agreement. This is a noteworthy achievement for the study of shocked solid-state samples, bringing state-of-the-art simulations and experiments into one-to-one comparison in temporal and spatial scales, without the need for any scaling. It is also a rather significant demonstration that these MD simulations using EAM potentials appear to be a reasonably good representation of experimental reality, provided very large scale simulations are undertaken.

V. Diffraction on Shocked Iron

The next dynamic diffraction experiments we describe were aimed at looking at phase, in particular, looking for solid-solid phase transitions. We show in Figs. 5a and 5b the first dynamic (time resolved) diffraction experiment to conclusively show the iron α to ϵ (bcc to hcp) phase transition at the lattice level in shocked iron.⁴¹⁻⁴³ The raw diffraction image for single crystal Fe shocked at 26 GPa along the [001] direction is shown in Fig. 5a, with the lattice planes identified. The diffraction arcs for unshocked material are labeled in blue. The arcs corresponding to elastically compressed bcc Fe are labeled in green, and the diffraction arcs corresponding to compressed hcp Fe are labeled in red. Peak uniaxially applied pressure vs. observed compression for an extensive series of shots for shocked single crystal Fe are plotted in Fig. 5b. Experiments from the Vulcan laser (red), Janus laser (green), and Omega laser (blue) are shown. For compressions up to $\sim 6\%$, the experimental diffraction data show that the crystal response is a 1D elastically compressed bcc lattice. Then there is a volume collapse, and the compression jumps to 15-18%, corresponding to the transition to an hcp lattice, consistent with the α - ϵ phase transition occurring for a shock strength of $\sim 13 \text{ GPa}$ (130 kbar). The time scale for this transition to occur is less than the $\sim 2 \text{ ns}$ time resolution of this experiment.

A set of large-scale MD simulations preceded the experiment,^{44,45} examples of which are shown in Figs. 5c and 5d. The simulation result (Fig. 5c) shows unshocked Fe (gray), a region of 1D uniaxial elastic shock compression (blue), and 3D relaxed hcp phase Fe (red), with grain boundaries shown in yellow, for a 15 GPa shock. Of particular note is that there is no plastic region in the shocked bcc Fe lattice. The elastically compressed bcc lattice transforms directly to the hcp relaxed Fe lattice, which is similar to what was observed in the laser-driven shock compression experiments shown in Figs. 5a and 5b. Figure 5d shows yet another important result from the MD simulations. The $\alpha - \epsilon$ transition for the 15 GPa shock in the MD simulations was very fast, requiring only $\sim 2 \text{ ps}$ to transform. The experiments also observed that this phase transition is fast, but only had $\sim 2 \text{ ns}$ time resolution, so could not establish how fast. Both simulation and experiment are consistent with a compression and shuffle mechanism responsible for the phase change from bcc to hcp.⁴² Also both show a highly-oriented nanocrystalline structure of very small grain size (grain sizes of 2-15 nm) after the phase transition, due to the four degenerate directions in which the phase change can occur.⁴⁶

Later experiments performed on polycrystalline iron⁴⁷ where the shock-induced phase transition was also observed, did show clear evidence for plasticity, presumably due to a combination of the effects of grain boundaries as sources of dislocations, and because the sample contained randomly oriented crystallites. It is also important to note that whilst MD

and experimental length and time-scales are now converging, the faithfulness of the simulations is dependent upon the fidelity of the potentials used, and in the case of shock compression, a good model of the system is required over a large range of compressions. This may explain why some predictions made by MD - such as a large fraction of fcc phase in iron shocked along other axes⁴⁵ - have not to date been seen experimentally.

VI. High Pressure Diffraction on Ramp Compressed Magnesium Oxide

Understanding the high pressure properties of MgO is of high interest, due to MgO being a common constituent of planetary interiors.^{49,50} Carrying out measurements at pressures of hundreds of GPa is very challenging. In this section, we describe two such experiments, one using a decaying shock technique with time resolved velocimetry (line VISAR) and pyrometry (SOP). The other used dynamic diffraction to look directly at the crystal structure, using a ramped compression drive to bring the sample to high pressure, but still in the solid state. First, the VISAR-SOP experiment, done on the Omega laser, where the MgO sample was compressed with a strong shock which was allowed to decay as a blast wave.⁵¹ The experimental configuration is illustrated in Fig. 6a. The analysis and interpretation of these experiments are presented as a temperature-pressure phase diagram for MgO at pressures from 0.0 – 0.8 TPa, as shown in Fig. 6b. The shock-compression experiments loaded the MgO samples to peak pressures of 1.4 terapascals (TPa), then allowed this blast wave to decay over a time interval of ~15 ns. By examining breaks in the slope of the temperature-pressure curves as the blast wave decays from 0.8 TPa down to 0.3 TPa, this group identifies the location of the liquid-solid transition at ~0.6 TPa, and the transition from the B2 (cesium chloride structure) to the B1 ((sodium chloride structure) phase spanning the range of ~0.35 – 0.45 TPa. The relevance and interest of these measurements for planetary science is illustrated by the brown curves in Fig. 6b corresponding to the predicted interiors of Earth, a “Super-Earth” (of 5 Earth mass size) planet, Jupiter, and a “Hot Jupiter” exoplanet.⁵¹ This group writes further that MgO is an electrically insulating solid up to melt, then becomes a metallic liquid above 0.60 TPa. They further suggest that the deep interiors of terrestrial planets can be electrically conductive, enabling magnetic field-producing dynamo action within oxide-rich regions and blurring the distinction between planetary mantles and cores.⁴⁸

We next describe a very high-pressure dynamic diffraction experiment for ramp compressed magnesium oxide (MgO), at peak pressures of up to 900 GPa (9 Mbar).⁵² These experiments were motivated by an interest to understand material properties and phases at the high pressures relevant to planetary interiors, including the newly discovered super-Earths.^{4,5} MgO was chosen as an important component of the Earth’s mantle and likely important for other planets. Little is known about the behavior of this oxide under conditions expected in the super-Earths with masses significantly greater than the mass of the Earth, where pressures can exceed 1,000 GPa (10 Mbar).⁶⁻¹⁰

The ambient phase of MgO is the NaCl-type rocksalt structure (denoted B1), and this phase is predicted to remain stable over a significant range in pressure and temperature.⁵¹ A phase transition from the six-fold coordinated B1 to the eight-fold coordinated CsCl-type (B2) structure is theoretically predicted in the 400–600 GPa range. With the existence of high energy lasers from ICF, these high pressure states of matter can now be experimentally probed. Experiments were carried out at the Omega Laser Facility, using direct laser illumination onto targets of 10- μ m-thick MgO powder pressed between two diamond “anvils”, as shown in Fig. 6c.⁵² The drive lasers used a temporally shaped laser pulse shape with intensity increasing over ~4.5 ns, producing a ramped pressure wave. A VISAR velocity interferometer recorded the free-surface velocity versus time at the back of the rear diamond anvil, establishing the pressure versus time

applied to the MgO sample. A Cu backlighter foil is irradiated using additional lasers with a 1 ns square pulse shape to produce quasi-monochromatic He- α radiation 8.3-8.4 keV incident at 45 deg. Diffracted x-rays are recorded in transmission geometry by image plates lining the inner walls of the diagnostic box, as shown in Fig. 6c.

The results from these diffraction experiments were analyzed to identify the lattice planes corresponding to the diffraction peaks, and to deduce the lattice spacing, as a function of pressure, as shown in Fig. 6d. These results show an abrupt change of lattice and spacing at 563 GPa, consistent with a phase transition from the B1 to B2. The MgO then remains in the B2 phase to the highest pressures achieved in these experiments, namely, 900 GPa.⁵² The density of the solid MgO up to 900 GPa was determined by assuming the B1 phase up to 563 GPa then the B2 structure at higher pressures. Previous experimental density measurements were limited to pressures of ~200–250 GPa for the solid phase, based on gas gun shock experiments and static x-ray diffraction. This data set extends the experimentally explored pressure range considerably, reaching 2.4-fold compression for solid MgO.

This work experimentally shows that a solid–solid phase transition, consistent with a transformation from B1 to the B2 structure, occurs near 600 GPa, and that the B2 structure remains stable to 900 GPa. The results shown are relevant to planetary science, because these conditions are expected to exist in the deep interiors of planets more massive than the Earth. This work also demonstrates that solid–solid phase transitions at these high pressures (600 GPa) can occur on short timescales (a few nanoseconds).

VII. EXAFS on Shocked Vanadium and Iron

We now discuss a time-resolved microscale diagnostic developed to probe the local lattice response, namely, dynamic extended x-ray absorption fine structure (EXAFS). This EXAFS technique probes the lattice short-range order, works both with polycrystalline or single crystal samples, and offers the potential to infer phase, compression, and temperature of the loaded sample, with sub-nsec time resolution.⁵³⁻⁵⁵ When an atom absorbs an ionizing, high-energy x-ray, an electron rises from a bound state into the continuum. The outgoing wave packet of the free electron scatters off of neighboring atoms. The outgoing and reflected waves interfere with each other. The square of the total electron wave function is what determines the probability of the process, and this interference is therefore observed in fine structure in the x-ray absorption just above an opacity edge. For K-edge absorption, the standard EXAFS equation can be written, in terms of the normalized absorption probability, as⁵³⁻⁵⁷

$$\chi(k) = \sum_j \frac{N_j}{kR_j^2} F_j(k) \sin\{2kR_j + f_j(k)\} e^{-2S_j^2 k^2} e^{-2R_j / l(k)}, \quad (2)$$

where $\chi(k) = [\mu(k) - \mu_0(k)] / \mu_0(k)$, and $\mu_0(k)$ represents the smooth absorption above the edge corresponding to an isolated atom (no interference modulations). The summation is over coordination shells, N_j is the number of atoms in the shell, and R_j its radius. The $F_j(k)$ factor corresponds to the backscattering amplitude for the electron wave function reflected from the j th coordination shell. The $\phi_j(k)$ represents a phase shift due to the electron wave packet moving through a varying potential. The exponential, $e^{-2S_j^2 k^2}$, represents amplitude damping due to the Debye-Waller factor, which reduces the coherent interference of the EXAFS signal due to thermal and static disorder fluctuations in the local scattering atoms,

and allows the lattice temperature to be measured, albeit volumetrically through the sample. The $e^{-2R_j / \lambda(k)}$ factor represents the attenuation of the electron wave function due to the finite mean free path, $\lambda(k)$, of the ejected electron.

A time-resolved EXAFS diagnostic technique has been developed at the Omega laser;⁵⁵⁻⁵⁷ the experimental setup is shown in Fig. 7a. Three 1-ns-square laser beams stacked back to back to make a 3-ns-square drive pulse are used to shock compress the sample being studied. The samples described here are either 10 μm thick polycrystalline vanadium or iron foils embedded in 17 μm thick CH tamper on either side, and the remaining 57 beams implode an inertial confinement fusion (ICF) capsule. This implosion generates a short (~ 150 ps) burst of smoothly varying hard x-rays, $I = I_0 \exp(-E_x/T)$, to be used for the EXAFS absorption.⁵²

EXAFS measurements from shocked polycrystalline vanadium at $P_{\text{shk}} \sim 35$ GPa, together with EXAFS theoretical fits, using the FEFF8 code,⁵⁶⁻⁵⁸ are shown in Fig. 7b. Vanadium was picked as a good reference material, since at that time it was not expected to undergo any phase transition at shock pressures $< \sim 100$ GPa. Subsequently a rhombohedral phase transition in vanadium was discovered at ~ 65 GPa,⁵⁹ but the new phase does not affect the results shown here. The fits of the shocked vanadium EXAFS data with the FEFF8 code shown in Fig. 7b are very good, and suggest a compression of $\sim 15\%$ and shock temperature of ~ 770 K. Both the shock compression and shock temperature thus inferred are in good agreement with predictions with radiation-hydrodynamics code simulations using the LASNEX code.⁶⁰

Shocked polycrystalline iron experiments were also done with this dynamic EXAFS technique.⁶¹⁻⁶² A 20% compression is predicted from radiation-hydrodynamics simulations of shocked Fe at $P_{\text{shk}} \sim 35$ GPa, assuming the $\alpha - \epsilon$ phase transition. The FEFF8 theory was used to establish the expected EXAFS spectra for unshocked α -phase (bcc) Fe and shocked ϵ -phase (hcp) Fe, assuming a $\sim 20\%$ compression for the shocked state. Figure 7c (red curve) shows the experimental result for shocked Fe, and clearly shows that the small peak marked “w” in the α -phase disappears in the ϵ -phase. Based on these results, the observed data are consistent with the $\alpha - \epsilon$ phase transition of shocked Fe, and that the transition time scale at $P_{\text{shk}} \sim 35$ GPa is $\tau_{\alpha-\epsilon} < \sim 150$ ps, where 150 ps is the time resolution of this measurement.⁵⁸⁻⁵⁹

VIII. High Pressure EXAFS on Ramp Compressed Iron

Dynamic EXAFS spectroscopy measurements have also been done on staged-shock ramp compression of iron up to 560 GPa (5.6 Mbar), as shown in Fig. 8a.⁶³ In these experiments, density, temperature, and local-structure measurements were made simultaneously for the compressed iron. The data show that the hexagonal close-packed (hcp) structure is stable up to 560 GPa. The temperature at peak compression is high and is explained as the result of a high dynamic strength of iron. These results also provide a constraint on the melting line of iron above 400 GPa.

The experiments were performed on the OMEGA laser and the broadband x-ray backlighter was generated by a spherical implosion. The target was a 4 μm thick Fe foil sandwiched between two diamond plates, each 35 μm thick, as shown by the experimental configuration in Fig. 8a. The diamond “anvils” confine the sample and maintain the pressure, thus creating a more spatially

uniform compression state in Fe. The applied stress versus time in the Fe sample, using a temporally shaped laser pulse shape, is determined by simultaneous VISAR measurements. The laser energy and the delay between the drive and the backlighter were varied in a series of experiments to probe different pressures and temperatures in the Fe. The pressure equilibration in the thin Fe samples is confirmed by hydrodynamic simulations using LASNEX⁶⁰. The short duration of the x-ray backlighter (~150 ps) ensures little temporal variation in the state of Fe during EXAFS measurements.⁵⁵

The temperature dependence of EXAFS measurements occurs through the Debye-Waller factor effect, as mentioned regarding Eq. 2.^{57,62,64-66} The temperatures obtained in the high pressure EXAFS data are shown in Fig. 8b as a function of stress in the Fe. The data indicate that off-Hugoniot states have been achieved up to 560 GPa and 8000 K. The data fall into two groups based on the compression history: single shock (blue diamonds), and leading shock stress of ~150 GPa followed by staged compression waves (black triangles). The two single-shock points agree well with the calculated Hugoniot. The staged shock data show higher temperatures compared to the isentropes calculated for ramp compression following an initial 150 GPa shock, but ignoring material strength, and lower temperatures than those for a single shock Hugoniot at the same pressure.

The measured temperatures are higher than those calculated for the isentrope in Fig. 8b due to the added heating caused by doing work against the solid-state material strength in Fe during compression at high pressure and strain rate. If one assumes that 100% of the work done against strength in compression goes into heat, the strength can be inferred from the measured temperatures. This is illustrated by the dotted and dashed black curves in Fig. 8b. The dotted curve fits the static strength results from 50 – 270 GPa pressures from Hemley et al.,⁶⁷ and extrapolates the fitted result to 600. The added heating from this analysis, is not enough to reproduce the experimental EXAFS temperature measurements. It is well known now that the strength of ductile metals increases significantly due to the high strain rates of dynamic compression, as will be discussed in the Sec. IX below.^{21,68-70} To better match the experimental data, the “dynamic strength” is approximated by multiplying the static strength by a constant factor treated as a fitting parameter. The best fit result, shown by the dashed curve in Fig. 8b, corresponds to a multiplier of 3, that is, $Y_{\text{dynamic}} \sim 3Y_{\text{static}}$. The inferred strengths were on the order of 60-80 GPa (600-800 kbar), at pressures from 200 – 500 GPa.

IX. High Pressure Material Strength Experiments

Beyond the important questions of the compressibility and the phase diagram of materials at high pressure, the shear flow behavior of materials has been the subject of increasing interest.²¹ The ability of a material to resist plastic (irreversible) flow is called material strength. Strong materials do not undergo plastic flow until higher stresses are applied. The vast majority of research on material strength has been near ambient conditions and at low rates. The shear stresses generated readily in plane-wave compression experiments using high-energy lasers or pulsed-power drives are more than sufficient to cause materials to yield. Once a material has yielded plastically, the strength of a material continues to be manifest in the flow stress, a measure of the shear stress during continued deformation. The flow stress is affected by the temperature and pressure, and it is also affected by the amount of the material has been strained plastically and the rate of deformation. The rise of the flow stress due to the accumulated plastic strain is known as work hardening. A well-known example is the increase in the strength of steel work hardened by a blacksmith hammering. The same effect occurs as metals are driven to high pressure in plane-wave compression. The initially one-dimensional loading in a planar compression wave induces a large shear stress that drives plastic flow and leads to significant

plastic strains.

There are a number of constitutive models that are widely used to calculate material strength (flow stress) in a fashion that can be incorporated into hydrodynamics continuum simulations. We will mention only four of the models used in the community. A more extensive review of the models can be found elsewhere.^{71,72} The Steinberg-Guinan model assumes that high-pressure, high-strain-rate strength can be approximated as the ambient strength multiplied by a pressure and temperature sensitive factor which is assumed to scale with the shear modulus, and a work hardening factor which is a power law function of strain.⁷³ The Steinberg-Lund model adds in an explicitly strain rate dependence, and explicitly includes the effects of thermal activation and phonon drag.⁷⁴ The Preston-Tonks-Wallace (PTW) model was developed specifically to address very high strain rate phenomena, and treats the thermal activation and phonon drag effects in a mathematically more sophisticated fashion.⁷⁵ And finally, the Livermore multiscale strength model (LMS), described in more detail below in Sec. IX.B, is based on information transfer from quantum density functional theory (DFT) to molecular dynamics (MD) simulations of dislocation mobilities, to dislocation dynamics (DD) simulations of the evolution of the full dislocation ensemble, finally to the continuum hydrodynamics scale.⁶⁵ As such, the LMS is more closely tied to first principles theory, but at the price of being much more computationally demanding to assemble or modify.

The strength of a material at high pressure is of interest because of the effect it can have on material dynamics. In the propagation of a plane wave, it is the longitudinal stress that enters the equations of motion, so it is not the pressure alone but the sum of the pressure and the shear stress that matters. Knowing the flow stress of a material provides this important addition to the equation of state (the pressure). The flow stress also affects hydrodynamic instabilities such as the Rayleigh-Taylor instability⁷⁶⁻⁷⁹ If a low-density material pushes against and accelerates a high-density material, the interface between the two materials is unstable to the growth of small perturbations, due to the Rayleigh-Taylor instability. Consider a layer of water above a layer of air. The low-density air pushes on the higher-density water due to gravity. Quickly small perturbations on the interface grow, and bubbles of air rise through the water as spikes of water fall through the air. The same effect can take place in solids as a low-density fluid accelerates a high-density solid, but the strength of the solid acts to reduce the effect, suppressing the growth of perturbations at short wavelengths and in some cases restoring stability. Rayleigh-Taylor instability is a potential source of detrimental mixing in ICF⁸⁰ and the use of strong materials may provide a means of controlling the mixing.⁷⁶

Several approaches have been developed to determine the strength of materials in high-pressure dynamic experiments. If the equation of state were known perfectly, the longitudinal stress determined by surface velocimetry (VISAR) would imply the flow stress. In practice, expressing the flow stress in terms of the difference of the pressure and the longitudinal stress relies on the difference of two large numbers, and uncertainties in the equation of state are often comparable to the flow stress: a more sophisticated technique is needed. Here we discuss three approaches to determining the flow stress that are designed to minimize the impact of uncertainty in the equation of state. The first approach uses the Rayleigh-Taylor growth of pre-imposed ripples on an accelerated interface to infer the flow stress. The second uses x-ray diffraction to measure the shear strain at the atomic level. The third measures the transit across the yield surface as the compression peaks and then the material releases. A forth technique was already discussed in Fig. 7b, where temperature is measured by dynamic EXAFS, and the heating beyond the isentrope is equated with the work done against the material strength (flow stress).⁶³

IX.A. Rayleigh-Taylor Strength Experiments

Dynamic material strength, which is a measure of the ability of a material to resist plastic deformation, has traditionally been studied in dynamic tests on a Split-Hopkinson Pressure Bar.⁸¹ In this technique, a well characterized plastic deformation is imparted to a specimen, which is analyzed to produce plots of stress vs. plastic strain as a function of strain rate and temperature. These results are compared with simulations including strength to test widely used constitutive models for strength. These techniques are limited to strain rates $< \sim 10^4 \text{ s}^{-1}$, and at applied uniaxial stresses of $\sim 1 \text{ GPa}$ (10 kbar) or less. The results that we describe below are typically at much higher pressures and strain rates, where until recently little to no experimental data existed.

Experiments to infer the flow stress at pressures of $\sim 100 \text{ GPa}$ have been conducted on metals at the Omega laser in Rochester and experiments have started at the National Ignition Facility. [Park 2015] The experiments use face-on x-ray radiography to measure the growth of pre-imposed ripples on the surface of the metal as it is accelerated by a material with much lower density. The configuration of the experiment is shown schematically in Fig. 9a. Laser beams enter a gold hohlraum where they generate an intense x-ray radiation bath. The x-rays strike a plastic ablator, generating a shock wave that runs through a graded-density reservoir composed of materials such as brominated plastic (BrCH). As the shock breaks out from the surface of the reservoir, it creates plasma that crosses a vacuum gap and stagnates against the plastic heat shield on the far side, in a technique first introduced by Barnes et al.⁷⁶ for high-explosive driven Rayleigh-Taylor experiments. The resulting ramp-compression wave accelerates the rippled interface between the plastic heat shield and the metal. The growth of these ripples is measured at an instant in time using x-rays generated from a metal foil as short-pulse laser beams from the Omega EP laser strike it. A LiF tamper is used on the back side of the metal sample to maintain high pressure.

The most thorough Rayleigh-Taylor (RT) strength experiments to date have been performed on the body-centered cubic metals vanadium^{82,83} and tantalum^{84,85}. In each case a series of experiments has been conducted keeping the drive constant but changing the timing of the backlighter to map out the time evolution of the growth of the ripples. The drive itself is determined from VISAR on a separate laser shot at the beginning of the day. The measured ripple growth factors for a series of Ta RT experiments with a peak pressure of 100 GPa (1 Mbar) are plotted in Fig. 9b. The growth factor is the ratio of the final ripple amplitude to the initial ripple amplitude, as determined from radiography (pR) using the procedure described in Park et al.^{82,83} The planarity achieved with the indirect (hohlraum) drive and the excellent performance of the micro-flag (foil) backlighter have enabled growth factor measurements with error bars less than 20%. The flow stress is inferred from the growth factor using a strength model, as explained in the next subsection, and a 20% uncertainty in the growth factor translates to a $\sim 20\%$ statistical uncertainty in the flow stress. Achieving this level of accuracy enables the determination of the effect of material strength on the hydrodynamics including hydrodynamic instabilities. A rather extensive series of experiments is overplotted, where the grain size of the Ta samples was varied. The Ta initial microstructures studied in these RT experiments corresponded to sputtered samples with columnar grain sizes of $\sim 0.25 \mu\text{m}$ lateral extent; wrought Ta with grain size of $\sim 10 \mu\text{m}$; wrought Ta with larger, $\sim 100 \mu\text{m}$ grains; [100] single crystal Ta; and [111] single crystal Ta. To within the error bars of the RT measurement technique, there were no observable effects of this grain size variation. In particular, a significantly enhanced strength, and reduced RT growth was not observed for the smaller grain sizes, due to the Hall-Petch effect.⁸⁵ The interpretation given is that at the very high strain rates of this experiment, $d\varepsilon/dt \sim 10^7 \text{ s}^{-1}$, the dislocation density (ρ_{disloc}) required to accommodate the plastic deformation is sufficiently high that Taylor (work) hardening, which varies as $(\rho_{\text{disloc}})^{1/2}$, dominates the other effects, including effects due to grain size (Hall – Petch).

IX.B. Multiscale Modeling of Strength Experiments

The RT experiments are not a direct measurement of strength, in the sense that it is not possible to take the observed ripple growth and do a simple calculation to determine the flow stress. Instead, the experiment is modeled with a continuum hydrodynamics code that uses a model for the strength (flow stress) of the metal. The ripple growth is greatest near peak pressure when the acceleration of the interface is greatest, but there is some growth at other times and the simulation is able to capture all of the accumulated ripple growth from the beginning to when the backlighter goes off. If the simulated ripple growth agrees with the measurements, the strength model is validated. In practice, several strength models have been used, as shown in Fig. 9b. The simulated ripple growth is greatest with no strength (top curve, blue), since there is no resistance to shear flow to slow the ripple growth. Comparison of this curve with the experimental data in Fig. 9b shows that the high-pressure material strength significantly reduces the RT growth. Simulations using the Steinberg-Guinan model⁷³ (second curve from the top, orange) and the Preston-Tonks-Wallace model⁷⁵ (middle curve, red) predict less growth than with no strength, but still growth that is several sigma too large. The simulations using the Livermore multiscale strength (LMS) model⁶⁸ agree with the growth factors from the experiment within the error bars (bottom curve, black). Both tantalum^{84,85} and vanadium^{82,83} RT experiments have shown that the strength at high pressure (~ 100 GPa) and high strain rate ($\sim 10^7$ s⁻¹) is a factor of 4-8 greater than the yield strength at ambient conditions, and in both cases the agreement with the LMS model has been good.

This agreement is remarkable since the LMS model was constructed starting from quantum mechanical first principles with essentially no empirical parameters, and specifically no parameters tuned to strength experiments. The model is a hierarchical multiscale model. It is constructed at the length scales known to be relevant to plasticity: calculations of the quantum mechanics of the electrons binding atoms together are used to construct effective atom-atom force laws without explicit electrons. The force laws are used in turn to determine the mobility laws dictating how lattice defects (dislocations) move under applied stress, as shown in the lower inset of Fig. 9c. An example of one of these dislocation velocity vs. stress curves is shown in Fig. 9c. The mobility laws are then used to calculate material hardening laws (how the flow stress increases as the material is work hardened and the plastic strain increases) using dislocation dynamics simulations that only track the defect positions with no explicit atoms. The resulting hardening laws and dislocation density limits (see the upper inset to Fig. 9c) are used in a continuum strength model suitable for hydrodynamic simulations, simulations that have no explicit electrons, atoms, or dislocations. There are many approximations made in the construction of the model, but no free parameters are left to tune to the experiment. The resulting agreement is remarkable.

The LMS model relates the flow stress to the temperature, pressure and plastic strain rate. It has dislocation density as a state variable that characterizes the microstructure of the metal. The initial dislocation density is input, and then it evolves in the model at each point in space according to the stresses and thermodynamic conditions. The model is time dependent at short time scales, which for Ta is at time scales of a nanosecond or less⁶⁹ It is possible to extract the density and average velocity of the dislocations from hydrodynamic simulations of the RT experiment, as shown in Fig. 9d. As *in-situ* characterization techniques are developed, it may become possible to test these predictions directly with experimental data. It is also possible to decompose the flow stress predictions from the multiscale model into the components (drag, thermal activation, and work hardening), as shown in Fig. 9e for the average conditions of the Ta-RT experiment and simulations shown in Figs. 9b and 9d, resp.⁸⁶ Such decompositions motivate

potential experiments to test the underlying assumptions of the multiscale model.

We show in Fig. 9f, the results from an analysis of Ta samples recovered after shock loading on the Omega laser.⁸⁷ The inset shows a TEM image for a single crystal Ta shock loaded along the [100] direction at an average shock pressure of 22 GPa, for a duration (“dwell time”) of < 50 ns. For this shock strength, the dominant residual microstructure from the plastic deformation appears to be dislocation loops, suggesting the deformation is via dislocation growth (“incubation”) and transport, collectively known as dislocation slip.⁸⁴

IX.C. In-situ Diffraction Strength Experiments

It is possible to determine the flow stress microscopically, at least for single crystal samples. The flow stress is a shear stress, related to local shear strains through the elastic constants: specifically the shear stress is the shear strain times the shear modulus, $\sigma_{\text{shear}} = G\epsilon_{\text{shear}}$. X-ray diffraction may be used to probe those shear strains at the level of the unit cell of the crystal lattice of the metal. That is, a metal consists of a regular lattice of atoms. For tantalum and vanadium, each atom is surrounded by eight nearest neighbors at the corners of a cube. Those cubic unit cells repeat in a regular lattice throughout the sample. The lattice is not perfect; there are point defects (vacancies and interstitials), line defects (dislocations) and other flaws in the crystal. Even in highly defective crystals, however, most of the atoms are surrounded by a cube of nearest neighbors, and that cube is only slightly distorted. The distortion is the shear strain at that point, and it may be probed using x-ray diffraction.

In-situ broadband Laue x-ray diffraction experiments have been carried out on shocked Ta foils at the Omega laser in Rochester,⁸⁸ as shown in Fig. 10a. The shock pressures ranged from 35 to 180 GPa (0.35 to 1.8 Mbar). Broadband Laue diffraction is only sensitive to shear strains in the crystal. Simultaneous VISAR measurements allow the applied longitudinal stress to be measured. With the Laue diffraction measurements, this allows shear strain to be measured vs. shock stress. The diffraction peaks are focused into individual spots on the image plate detector. Hydrostatic compression would leave the spots unshifted from their ambient positions. On the other hand, shear strain shifts the positions of the spots, as shown in Fig. 10a. Measuring that shift gives the shear strain ϵ_s and, if the shear modulus G is known, the shear stress (flow stress) $\sigma_{\text{shear}} \sim G\epsilon_{\text{shear}}$ can be deduced, as shown in Fig. 10b. In the shocked Ta experiments, the shear stress was found to vary from ~10 GPa to ~35 GPa as the pressure was increased from 35 to 180 GPa (0.35 to 1.8 Mbar). These strength values are high, in agreement with the LMS model extended to include shock heating and to account for homogeneous nucleation of dislocations at the high strain rates at the shock front.⁸⁸

IX.D. Ramp Compression/Release Strength Experiments

Another approach to determining the strength of metals at high pressure has been developed by Asay et al.⁸⁹ and Brown et al.,⁹⁰ and used at the Z machine, a pulsed power facility, to determine the strength of Ta in the pressures up to 250 GPa (2.5 Mbar). Here the samples are typically somewhat larger and the strain rates $\dot{\epsilon}$ somewhat lower than in the laser experiments: samples 900-2000 microns thick vs. 30-50 microns thick, and $\dot{\epsilon} \sim 10^5$ - 10^6 /s vs. $\sim 10^6$ - 10^7 /s for the laser. Magnetic loading was used to take the samples up to the pressure of interest in either the co-axial configuration or the stripline configuration shown in Fig. 11a. In either case a time-varying magnetic field interacts with the current running through the anode on which the samples are mounted, inducing a Lorentz force. The variation in time of the magnetic field is designed to drive a wave that ramps the pressure to a peak and then release it gradually. VISAR measures the resulting surface velocities for both drive measurements and strength measurements in the same

shot.

The principle of the experiment introduced by Asay and Lipkin⁹¹ is to calculate the shear stress from the Lagrangian sound speeds as the longitudinal stress peaks and releases during which time the material behaves elastically. As the pressure is ramped up the material yields, and the shear stress in the plane-fronted wave is pinned to the yield surface. As the stress peaks and begins to decrease, the shear stress drops inside the yield surface so the response is elastic and eventually goes sufficiently negative to hit the other side of the yield surface. With a number of common assumptions such as simple wave behavior, it is possible to determine the Lagrangian sound speed at points inside the sample from surface velocity (VISAR) measurements. Those Lagrangian sound speeds are then used to determine the change in shear stress crossing the yield surface and thus provide an approximation to the flow stress on loading.⁹⁰

The longitudinal stress vs. strain curves from a series of experiments loading Ta from 60 to 250 GPa (0.6 to 2.5 Mbar) were measured, along with a curve generated from the SESAME 90210 equation of state. The inferred flow stress Y vs. pressure is plotted in Fig. 11b. As may be seen in Fig. 11 of Ref.,⁹⁰ the Ta flow stress measurements generally agree with earlier dynamic measurements and the SG and PTW models at pressures below 60 GPa (0.6 Mbar), but become stiffer than those models at higher pressures. Figure 11b in this paper is based on the high-pressure part of Fig. 11 of Ref. 90, but improved by using an improved non-linear optical model for the LiF window at pressure. The figure shows results from simulations using the LMS model, the Steinberg-Lund model, the PTW model and the Steinberg-Guinan model, for comparison. The LMS model provides the best approximation to the data from the Z machine at these higher pressures, somewhat under-predicting the strength at the highest pressures. The other models predict lower strengths. The PTW and Steinberg-Lund models are in good agreement with the Starck data at lower pressures, but substantially under-predict the strength at the highest pressures. The data for the cold rolled and sputtered samples show a higher strength, and this material processing dependence is not accounted for by any of the models. The variation is attributed to a dependence of the flow stress on the initial microstructure⁹⁰ an observation which differs from that of the laser driven Ta Rayleigh-Taylor strength experiment at higher strain rates, shown in Fig. 9.

X. Shock Vaporization of Silica

Understanding shock-induced melting and vaporization is important for developing realistic models of planetary formation dynamics.⁹² In particular, it is thought that the formation of planets and planetary systems involves energetic collisions between planets and planetessimals. For example, the last giant impact is thought to explain the diverse characteristics of the planets in the Solar System⁹³ including the large core of Mercury,^{94,95} formation of Earth's moon⁹⁶ and Pluto's moons⁹⁷ These collisions attain shock pressures that result in significant levels of melting and vaporization. Yet accurate understanding of shock-induced melting and vaporization for planetary constituent materials is lacking. Planetary collisions are particularly challenging to model because of the need to understand both the extreme temperatures and high compression ratios achieved in the shocked states and the low densities and temperatures of the shock-vaporized material on release. Experiments are required to constrain the equation of state throughout the phase space traversed in modeling these planetary impact and release impact dynamics.

The irreversible work from shock compression can be dissipated as heat through an increase in either temperature or entropy, where the balance between temperature and entropy depends upon the heat capacity. One of the methods used in the planetary community for predicting the amount

of melting and vaporization that occurs during planetary impact events (as well as in strong shock and release experiments in the laboratory) is the so-called “Entropy Method”.⁹⁸ The technique assumes that a strong shock upon breaking out through a free surface will release into vacuum along an isentrope. Since the leading edge of the releasing material is at ambient pressures, standard laboratory experiments can establish the entropy there, for a given temperature. Then if the release dynamics, namely, density and temperature as a function of the distance of release, can be determined, one can use the isentropic release to set the entropy behind the shock prior to shock break out.⁹²

The experimental configurations used at the Janus laser for these shock entropy experiments in silica are shown in Fig. 12a. In a configuration similar to this, but without the LiF window, experiments measured the shock strength as the shock traverses the quartz sample, and gave the shock strength and temperature at shock breakout from the quartz free surface. The diagnostics were a streaked line VISAR and a streaked optical pyrometer (SOP).⁹² These experiments were followed with experiments where the shocked quartz released across a known vacuum gap thickness, then stagnated on a LiF window, which is the configuration shown in Fig. 12a. Since the shocked quartz releases as a liquid-vapor mixture, its density drops monotonically as this mixture releases across the gap until it stagnates and accumulates on the LiF window. The result is a ramped compression wave moving into the LiF window. The gap size and shock strength were varied in a series of experiments, and the temperature and density of the releasing SiO₂ mixture of liquid and vapor was determined.

The combined analysis of these two variations of the Janus experiments allowed the experimental temperature-entropy plot to be created, as shown in Fig. 12b. To interpret the observed post-shock temperatures, a model was developed for the apparent temperature of a material isentropically decompressing through the liquid-vapor coexistence region. Using published thermodynamic data, the liquid-vapor boundary for silica was modified based on these experiments and finally the entropy on the quartz Hugoniot was calculated, shown by the open circle plotting symbols. Note the shape of the liquid-vapor curve in Fig. 12b (the gray continuous curve with a peak at entropy of ~5000 J/kg/K). At the highest entropies (strongest shock strength), the temperature of the releasing, co-existing liquid-vapor SiO₂ is dropping, due to an increase in the fraction of liquid that has vaporized (and the internal energy absorbed due to the latent heat of vaporization). At the lowest shock strengths in the quartz, the temperature of the releasing SiO₂ is lower, due to the lower internal energy deposited into the quartz from the weaker shock. This leads to the peaked T-S shape often referred to as the “vapor dome”.

The impact of these experiments are revised critical shock pressures for vaporization which are lower than previously estimated, primarily due to the revised entropy on the quartz Hugoniot. As the thermodynamics of other silicates are expected to be similar to quartz, it is concluded that vaporization is a significant process during high-velocity planetary collisions. For a given shock strength, a higher fraction of vaporization is expected upon release, using the adjusted liquid-vapor boundary resulting from these experiments.

A more recent experiment on the Omega laser, using the technique of a decaying blast wave,⁹⁹ the high pressure shock Hugoniot, temperature, and conductivity of a decaying shock in fused silica, quartz, and stishovite was measured. The experimental configuration is illustrated in Fig. 12c.¹⁰⁰ The primary diagnostics used were a velocity interferometer (VISAR), and a time resolved, absolutely calibrated optical pyrometer (SOP). The conclusions from these experiments and subsequent analysis and simulations are illustrated in Fig. 12d. Also indicated in Fig. 12d are the temperature-pressure locations of the core-mantle boundaries of Earth, Uranus, and Neptune. The temperatures vs. shock strength up to ~700 GPa are given. The discontinuities in these curves are

used to infer the transition from solid to liquid. The overall result is a new calculated high pressure SiO₂ melt curve, calibrated to the experimental measurements. Further, it was shown that in the high pressure liquid state, the SiO₂ is nearly as conducting as iron, which suggests that silicates deep in planetary interiors might also participate in the dynamo generation of magnetic fields. This in turn suggests a need to include multiple layers of conductive fluids in planetary interior models, in particular, in the context of whether magnetic fields are formed.

XI. Properties of Carbon at pressures up to 5 TPa (50 Mbar)

The high pressure properties of carbon (and other materials) are of significant interest to inertial confinement fusion,^{12,13} planetary science, particularly as it relates to planetary interior structure;¹⁰¹ and planetary formation dynamics;^{93,96,97,102,103,104} and to asteroid and meteor impact dynamics.¹⁰³⁻¹⁰⁷ In this section, two experiments that probe the high pressure properties of diamond (carbon) are described, one using a decaying shock technique on the Omega laser,⁹⁶ and the others using ramp compression of diamond on the NIF laser.¹⁰⁸

The Omega decaying shock (blast wave) experiment is illustrated in Fig. 13a. Here, direct drive laser focused onto a parylene ablator launches a very strong blast wave through an aluminum “piston”, and then into the 500 μm thick diamond sample. The shock velocity and temperature at the shock front are measured with velocity interferometry (VISAR), and time resolved optical pyrometry (SOP).⁹⁹ The measured shock velocity vs. time in the diamond is shown at the bottom of Fig. 13a. The experimentally determined temperature versus pressure resulting from these experiments, along with comparisons to simulations, are shown in Fig. 13b. The black curve corresponds to this Omega experimental data. The blue circles and blue dashed curve correspond to the theoretical melt curve from density functional theory,¹⁰⁹ whereas the brown triangles and brown dashed curves represent theoretical calculations by Correa et al.¹¹⁰ These data are further analyzed to produce the specific heat, C_V , of carbon at these high pressure conditions, and the authors conclude that the observed peak in C_V is likely due to a reconfiguration of packing, from a partially bonded complex fluid to an atomic fluid above 60,000 K. This group also relates their results to the concentrations and distributions of carbon in Neptune and Uranus.

Recently experiments have been developed using the ~ 2 MJ National Ignition Facility (NIF) laser at LLNL to study the properties of matter at many tens of megabar pressures. The first of these experiments used the very precise laser pulse shaping capability of the NIF laser, which was developed partly to drive ICF capsule implosions to very high densities for fusion energy research. The same type of pulse shaping for the 192 NIF lasers focused into a standard NIF ICF radiation cavity (“hohlraum”) was refined to drive a planar diamond (carbon) target mounted on the wall of the hohlraum (as opposed to a spherical capsule located at the center of the hohlraum), to probe the very high pressures relevant to planetary and brown dwarf interiors.¹⁰⁸ The theoretical description of such electron-degenerate matter has recently suggested that new complexities can emerge at pressures where core electrons (not only valence electrons) influence the structure and bonding of matter. This new experimental work describes ramp-compression measurements for diamond, reaching nearly 4-fold compression at a peak pressure of 5 terapascals (50 Mbar). These data can now be compared to first-principles density functional calculations and theories long used to describe matter present in the interiors of giant planets, in stars, and in inertial-confinement fusion experiments. These data also provide new constraints on mass–radius relationships for carbon-rich planets.⁸

The experimental configuration used for these high-pressure ramp compression experiments on NIF is shown in the inset of Fig. 13a. A highly shaped laser pulse is generated by focusing 176 synchronized, 20 ns duration laser beams into a hollow cylindrical Au radiation cavity, called a

hohlraum, converting to a temporally shaped radiation temperature, $T_r(t)$ vs. time. A hole is cut into the side of the hohlraum wall, and a planar physics package, consisting of a 50 μm synthetic diamond ablator, a 10 μm Au x-ray preheat shield, and 4 precision steps of synthetic diamond, is mounted over this hole. The shaped radiation drive launches a ramped compression wave through these diamond steps, and the free surface velocity vs. time, $u_{fs}(t)$, is measured as the waves break out of the back side using a streaked line VISAR diagnostic, as shown in Fig. 13a. The free surface velocity profiles shown in Fig. 13a are analyzed by an iterative Lagrangian method developed by Rothman,¹¹¹ to generate the stress-density results for carbon shown in Fig. 13b. For reference, the pressures at the center of Earth, Neptune, and Saturn are indicated on the vertical axis by the red arrows.

This stress-density result for carbon, which is thought to remain solid throughout the ramped compression wave, can be compared with the results of a number of equations of state (EOS) models in the multi-terapascal regime. Comparisons to a density functional theory (DFT) calculated cold curve, and a DFT Hugoniot curve are shown by the dashed and solid red curves, respectively. These two curves, based on quantum mechanical theory and taking into account the lattice structure of the carbon, bracket the experimental data on either side. The DFT Hugoniot predicts the carbon to be liquid at the higher stresses ($> \sim 1$ TPa), and less compressible than observed. The DFT cold curve, however, predicts the carbon to be more compressible than observed, and also predicts two phase transitions, which appear as stress plateau kinks in the otherwise smoothly rising stress-density curves: diamond to BC8 at ~ 0.99 TPa and BC8 to simple cubic at ~ 2.7 TPa. Neither of these two kinks is apparent in the experimental data, which remains very smooth throughout the compression. It may be that kinetic effects due to the high rates of compression smooth out these phase transition kinks. Or it may be that, due to the short time scales of the experiments, the phase transitions have not yet had time to complete themselves. Additional experiments on NIF continue to explore the high-pressure properties of carbon. What is clear is that the experimental data are less compressible than the DFT cold curve, more compressible than the DFT Hugoniot, and do not show the traditional stress-density discontinuities (plateau kinks) typically seen from phase transitions. The peak stresses achieved exceed those at the centers of Earth (360 GPa), Neptune (~ 800 GPa), and Saturn (~ 4 TPa), thus opening up a new capability of probing material properties at conditions matching the deep interiors of giant planets.¹⁰⁸

XII. Material properties at 100 TPa (1 Gbar)

To study the properties of matter at the highest pressures (~ 100 TPa or 1 Gbar) and densities requires spherical convergence. We describe a NIF experiment under development to probe matter, and measure the equation of state, in a shocked converging solid sphere of low-Z material. The materials being studied in this development project are CH, CD, and diamond (carbon). A schematic of the experimental setup is illustrated in Fig. 14a.^{112,113} Here solid targets of CH or CD are shock compressed using a hohlraum radiation source. The plasma is probed with x-ray radiography in the equatorial direction and x-ray scattering in the polar direction. A wedged cross-section of the solid CH target with a Ge doped CH ablator is shown on the upper left, giving the radii of the layers, and the percent dopant of the Ge layers. The Ge layers are to block the M-band hard x-rays from the hohlraum drive from preheating the solid CH sphere that is being shock compressed.

The experiments and data analysis are still in progress. The design point being pursued, however, is illustrated with the pressure – radius plot shown from the design simulations in Fig. 14b.¹¹³ Pressure as a function of shock radius is given for simulations using equation of state LEOS 5350 (red), LEOS 5400 (green), and Sesame 7592 (black). Note that to reach pressures of ~ 1 Gbar

requires convergences down to radii $< 100 \text{ } \mu\text{m}$. The inset of Fig. 14b shows a simulated radiograph for 9 keV x-rays as a function of time and capsule radius. Here, the integrated transmission is convoluted with the backlighter function in time and space. Also plotted is the location of the predicted self-emission flash. Fiducial wires are used to determine the magnification of the instrument and a 4ω fiducial is used to determine the absolute diagnostic timing. The challenges posed by measurements at these maximal convergences are (1) the finite spatial and temporal resolutions of the diagnostics start to have a significant impact; (2) the self emission flash may potentially start to be a source of background; and (3) at the highest convergences and pressures, the Ge preheat shield layers have been burned through, and the CH sample being studied is at risk of being preheated by the hard x-ray component of the drive.

The final aspect of the Gbar experiments currently being carried out on the NIF laser is to experimentally measure the density and temperature of the dense plasma at the conditions of interest. An x-ray Thomson scattering (XRTS) diagnostic is under development on NIF to carry out these plasma characterization measurements at very high plasma pressures and densities,¹¹⁶ under similar conditions as shown in Fig. 14. At the time of this writing these NIF XRTS plasma characterization experiments are just starting. Extensive development work has been done on other lasers around the world, however, such as the Omega Laser Facility at LLE in Rochester, NY, and the nhelix laser system at GSI in Germany.¹¹⁷ The experiments done at nhelix are illustrated in Fig. 15a, showing a 65 J, 11 ns, 1ω drive laser launching a shock through a graphite sample, and a planar titanium foil, driven by a 150 J, 1 ns, 2ω laser used as the $\sim 5 \text{ keV}$ backlighter source for the XRTS measurements.¹¹⁸ Figure 15b shows the measured spectrum at a scattering angle of 126° , showing distinct, reasonably narrow elastic scattering features (green dashed curve), the inelastic scattering component (red dot-dashed curve), the combined result (solid dark blue curve), and the experimental data (gray dots). These data are then analyzed to extract the atomic form factor (also called the ion-ion density correlation function), S_{ii} ,¹¹⁸ which is plotted as a function of wave number, and compared with a number of leading theories, and MD simulations. The results of these theoretical fits allows a plasma density, temperature, and pressure to be deduced, even at these dense, high pressure (100-200 GPa), warm dense matter (WDM) plasma conditions. Of particular interest is that these experimental conditions are similar to those found in the interiors of planets. These results presented in Kraus et al. confirm the structure predicted by *ab initio* quantum simulations and demonstrate the importance of chemical bonds at extreme conditions similar to those found in the interiors of giant planets, such as the carbon-bearing icy giants Neptune, Uranus, and a number of the extrasolar planets.

XIII. Conclusion

With modern high energy density (HED) experimental facilities, such as high-power, high-energy lasers, pulse power magnetic pinch facilities, and advanced light sources coupled with capabilities to launch shock waves into samples, matter can now be studied experimentally with precision at very high pressures and over very short time scales. Laboratory studies can now be conducted on the basic properties of matter, such as phase, strength, conductivity, and ductility at conditions matching those of planetary interiors, including the now more than 1000 discovered exoplanets.^{4,5} Furthermore, the time response to matter as it is being compressed can now be measured down to sub-picosecond resolution, and over micron spatial scales. For the first time, this allows quantitative direct one-to-one comparisons of experimental data with molecular dynamics simulations, whose interatomic potential is tied to quantum mechanics. Also, new multiscale theoretical models now can simulate macroscopic material response with

information passing methodologies that allow direction connection back to quantum based interatomic potentials. With these modern experimental and theoretical capabilities, the pace of new discoveries in the properties, phases, and states of matter is accelerating, which highlights one of the most exciting eras in science. And in particular, coupled with the studies of planetary formation, the formation of planetary systems, and investigations of the likely environments in, on, and around the exoplanets, these new experimental and theoretical capabilities are tied to far reaching explorations about the universe.

The combination of high energy, high power laser and pinch facilities, and next generation light sources means that new high energy density (HED) phases of matter are sure to be discovered, and phase transition pathways decoded. Another frontier area of HED science just starting to be examined experimentally is the onset of “keV chemistry” in WDM at exceedingly high densities and pressures, where the chemistry is determined by the inner shell, more tightly bound electrons.¹²⁰ With new generations of diagnostics on HED facilities rapidly being developed, such as x-ray Thomson scattering to establish the plasma conditions (T_e , n_e , n_i , v , ionization state), time resolved *in situ* diffraction to measure the lattice structure in solids, dynamic EXAFS to probe the local structure at the atomic level, x-ray backlighting at extraordinarily high fluences and temporal and spatial resolution, and most recently, proton radiography to measure time and spatially resolved electric and magnetic fields generated in HED matter, this area of science is poised to experience exponential rates of progress and discovery in the coming years. Increased shot rate, diagnostics with multiple lines of sight or broader angular coverage, diagnostics with many time frames per shot, higher diagnostic signal to noise and signal to background ratios, and new approaches to making sophisticated precision targets more efficiently and economically all are challenging areas of current effort, and where progress will be highly beneficial for the field. For experiments done at small spatial and temporal scales, there is effectively one-to-one overlap with advanced and new simulation capabilities, including molecular dynamics (MD), collisionless and collisional particle in cell (PIC) simulations. For the experiments that reach the highest pressures and densities, in that sense, the most novel states of matter, however, new hybrid simulation techniques are needed to combine MD, PIC, and/or hydrodynamic techniques to be able to increase the range of spatial and temporal scales accessible with such state of the art simulations. In general, the connection between theory (through simulation) and experiment is very tight, with experiments driving theory and theory motivating new experiments. This is an exiting field, and an exceptionally exhilarating time to be involved in this area of research.

Figure Captions

Figure 1. Iron at high pressure and high rates. (a) The trajectory of shock and shock-ramp experiments superimposed on the iron phase diagram and plotted along with the range of possible temperatures for the Earth’s interior (orange curve). These experiments demonstrated that the α - ϵ Martensitic phase transition at ~13 GPa can be overdriven by a leading shock to eliminate time-dependent material response and a growing shock during the subsequent ramp compression. (Adapted with permission from Ref. 3.) (b) The free surface velocity as a function of time (normalized to sample thickness) for iron driven to 23.7 GPa in a gas gun experiment, showing a multiple wave structure due to the α - ϵ phase transition and wave interactions. (Adapted with

permission from Ref. 22.) (c) Free-surface velocity versus time from a ramp wave, uniaxial loading experiment on iron at the Sandia Z-machine. The inset shows the time-dependent decay of the velocity plateau associated with the $\alpha - \epsilon$ phase transformation. (Adapted with permission from Ref. 24.) (d) A compendium of experiments using ramp wave compression of iron, and plotting the $\alpha - \epsilon$ transition stress as a function of strain rate associated with the phase transition, $(d\mu/dt)_{\alpha-\epsilon}$. Inset: Peak elastic stress versus strain-rate at the onset of plastic flow in Fe. The data of Crowhurst and Armstrong was obtained on $\sim 1 \mu\text{m}$ thick Fe samples driven with a $50 \mu\text{J}$, ~ 270 ps, 800 nm wavelength short pulse, Ti:sapphire table-top laser.²⁸ The different plotting symbols correspond to different experimental conditions and facilities, as described in Ref. 24. (Adapted with permission from Ref. 24.) (e) Experimentally determined sound velocities of iron as a function of pressure from this study (solid circles) in comparison with results from previous experiments. See Ref. 26 for details. The tip and bar along the upper edge show the pressure at the inner core boundary (ICB) of Earth and the pressure range at super-Earth's core, respectively. The lower right inset shows the trajectories of the front and back surfaces of the driven iron foil. (Adapted with permission from ref. 26.) The upper left inset is a schematic illustrating the shock and rarefaction trajectories. (Adapted with permission from Ref. 27.) (f) The Pressure - Temperature diagram of iron from *ab initio* calculations. The colored curve is the thermodynamic path measured in the experiments described in Ref. 28, showing compression up to 700 GPa then release along the isentrope. The thick black curve shows the numerical simulation of the experiment. The thin black curve is the SESAME Hugoniot (Iron #2150). The gray band represents the error bars on the experimental measurement. The thermodynamic path closely follows an isentropic compression after the initial shock precompression. (Adapted with permission from Ref. 28.)

Figure 2. (a) A schematic representation of the experimental setup for a dynamic diffraction experiment showing schematically the x-ray diffraction signal from the (1) unshocked and (2) shocked single crystal Si. (Adapted with permission from Ref. 32.) (b) Diffraction results from Si unshocked and shocked to 6.7 GPa (67 kbar) where the shock propagation direction was along the [111] crystallographic direction, and the streaked (time-resolved) diffraction was from the (111) lattice planes. (Adapted with permission from Ref. 32.)

Figure 3. (a) A schematic of the experimental setup (center), along with time integrated transmission Bragg diffraction from (040) Si lattice planes (left side) and reflection Bragg diffraction from (400) Si lattice planes (right side). (Adapted with permission from Ref. 33.) (b) Time-resolved x-ray streak camera image of the reflection Bragg diffraction signal shown in Fig. 1a. The diffraction angle and corresponding compression of the (400) lattice are shown as a function of time with respect to the start of the drive laser. (Adapted with permission from Ref. 33.) (c) Profiles of the time-integrated Bragg diffraction signals from shocked single-crystal Si in the reflection (400) geometry, and (d) in the transmission (040) geometry. (Adapted with permission from Ref. 33.) In (c) and (d), the upper traces correspond to the shot shown in (a) and (b), with a peak compression of 6.2%, the middle traces for a shot with similar peak compression, but slightly different drive history, and the lower traces for a shot with peak compression of 11%.

Figure 4. (a) Dislocation structure resulting from a molecular dynamics (MD) simulation of copper shocked in the [100] direction. The image shows a snapshot from a simulation with a 50 ps rise time for the linearly ramped piston velocity, at $t \sim 100$ ps, showing only dislocation atoms. The copper crystal included pre-existing dislocation sources. The color is only to enhance the view of the dislocations. The three regions of dislocation activity—multiplication, mixed and homogeneous nucleation—are marked. (Adapted with permission from Ref. 37.) (b) Response of the MD lattice during 3D plastic relaxation. The relaxation of the shear stress inferred from

simulated x-ray diffraction, as a function of time behind the shock front. The black horizontal dashed line indicates the value for full 3D relaxed compression. The red curve corresponds to the 0 ps rise-time shock case, and the blue curve to the 50-ps ramped case. (Adapted with permission from Ref. 37.) (c) Experimental configuration for the LCLS experiment measuring the shock response of a 1 μm thick shocked Cu polycrystalline sample with a preferential [111] orientation. The lattice response was captured in a Debye-Scherrer geometry by a series of 48-fs snapshots. (Adapted with permission from Ref. 39.) (d) Simulated diffraction profiles, which were in good agreement with experiment, show the evolution of the lattice response in 20 ps steps from the unshocked lattice to the elastic precursor compression, and the plastic relaxation of the compressed lattice. (Adapted with permission from Ref. 39.) (e) Calculated elastic and plastic strain vs. time at a sample depth of 200 nm. Note that the plastic relaxation (plastic strain) does not begin until the normal elastic strain reaches a peak value of $\sim 18\%$. (Adapted with permission from Ref. 39.) (f) Stress-strain curves from MD simulations of shocked Cu along the [123], [110], and [111] directions (left vertical scale), and [001] (right vertical scale) at 300 K and strain rate of 10^8 s^{-1} . The strain threshold for dislocation nucleation (onset of plasticity) is indicated with arrows. (Adapted with permission from Ref. 40).

Figure 5. (a) Sample image of the diffraction data from reflection for shocked single crystal iron for a 26 GPa (260 kbar) shock in the [001] direction. Diffraction from the static bcc lattice is shown in blue, from the elastically compressed bcc lattice in green, and from the hcp phase in red. (Figure 5a is adapted with permission from Ref. [41]. Copyrighted by the American Physical Society.) (b) Volume of the compressed iron plotted vs peak drive pressure. Solid points represent the peak compression observed, and open points represent the lower compression observed for each experiment. Results from postprocessed MD simulations (black circles), and the room temperature shock Hugoniot (gray curve) are shown overlaid. (Figure 5b is adapted with permission from Ref. [41]. Copyrighted by the American Physical Society.) (c) MD simulation of shocked iron (shock fronts propagate from left to right) after 8.76 ps in the bcc [001] direction for a shock strength of 471 m/s ($u_p = 471 \text{ m/s}$, $u_p/c_0 = 0.0951$, $P_{\text{shk}} \sim 15 \text{ GPa}$). Atoms are color-coded by the number of neighbors n within 2.75 \AA . Gray, unshocked bcc ($n = 8$); blue, uniaxially compressed bcc ($n = 10$); and red, the transformed close-packed grains ($n = 12$) separated by yellow ($n = 11$) grain boundaries. This shock strength is just above the α - ϵ transformation threshold. (Adapted with permission from Ref. 44.) (d) Nucleation of close-packed (hcp) material in the shocked [001] Fe at $P_{\text{shk}} \sim 15 \text{ GPa}$, which is just above the α - ϵ transformation threshold. Only atoms with a transverse movement above 0.42 \AA are shown and colored by their transverse displacement [gray = 0.42 \AA , cyan = 1.32 \AA (about half the nearest neighbor distance)]. After 1.095 ps (left), small nucleation centers start to grow along close-packed planes and finally build the transformation front (right, after 2.19 ps). (Adapted with permission from Ref. 44.)

Figure 6. (a) Schematic of an experiment on the Omega laser using the decaying shock technique. The planar target corresponded to a 10 μm CH ablator, followed by an Al “piston”, then the MgO sample under study, and backed with a thin anti-reflection coating. The primary diagnostics were a streaked line VISAR and a streaked optical pyrometer (SOP). (Adapted with permission from Ref. 51.) (b) The pressure – temperature phase diagram for MgO. The experimental data from the Omega experiments are shown by the solid red and blue symbols with error bars. The open black circles are from gas gun experiments and the solid dot-dashed curve is a theoretical estimate, both from Ref. 111. The proposed phase diagram resulting from this Omega experiment is shown by the heavy black curves. Zero-temperature B1-B2 transition pressures from theory are given by the gray bracket. The expected conditions for the planetary interiors of

Earth, a 5 earth mass Super Earth, Jupiter, and a hot Jupiter-mass planet are given by the brown curves. (Adapted with permission from Ref. 51.) (c) Experimental set-up for powder X-ray diffraction from ramp-compressed MgO samples at higher pressure at the Omega Laser Facility, showing the diagnostic box containing image plates and target assembly sitting in the front plate. X-rays generated by laser illumination of a Cu foil hit the bottom plate and the diffracted signal is recorded on the other panels (red lines indicate example diffraction at $2\theta = 55^\circ$). Additional lasers compress the target, and VISAR measurements allow a pressure determination. . (Adapted with permission from Ref. 52.) (d) Comparison of measured d-spacings in diffraction from the ramp compressed MgO on Omega (gray solid circle plotting symbols) with diamond anvil cell (DAC) experiments (black and red curves) and simulations (dashed blue and dot-dash black curves) below and above 563 GPa for B1 and B2 phase MgO. (Adapted with permission from Ref. 52.)

Figure 7. (a) Schematic of the experimental configuration for dynamic EXAFS measurements for shocked vanadium and titanium on the principle Hugoniot. The imploding spherical target serves as a continuum x-ray backlighter “point” source for the EXAFS measurements. The three-stacked 3ω laser beams launch a shock through the $10\ \mu\text{m}$ sample tamped on both sides with $17\ \mu\text{m}$ of CH. (Adapted with permission from Ref. 57.) (b) Fitting the measured V EXAFS spectra for the shocked V experiment with the FEFF8 code. (Adapted with permission from Ref. 57.) (c) Experimental EXAFS results for unshocked and shocked iron. The disappearance of the peak marked “w” is a signature of the α to ϵ phase transformation. (Figure 7c is adapted with permission from Ref. [61]. Copyrighted by the American Physical Society.)

Figure 8. (a) Schematic of the experimental configuration for dynamic EXAFS measurements on iron for off-Hugoniot staged-shock loading to peak pressures approaching 600 GPa. (Figure 8a is adapted with permission from Ref. [63]. Copyrighted by the American Physical Society.) (b) Temperature inferred from the Debye-Waller factor (DWF) in the dynamic EXAFS data for Fe as a function of stress for the staged shock drive with an initial shock of ~ 150 GPa followed by ramp compression waves up to 570 GPa. The single-shock data are also shown (blue diamonds). The melting curve (dot-dot-dashed lines) and the Hugoniot (green solid lines with dots) are plotted for comparison. Also shown are isentrope curves following the 150 GPa shock for the no-strength case (solid black curve), for a calculation assuming strength based on static data, Y_{sta} (dotted lines), and for a calculation assuming “dynamic strength” is a factor of 3 greater than static strength, $Y_{\text{dyn}} = 3Y_{\text{sta}}$ (dashed lines). Including Fe strength in the analysis increases the temperature due to the work done against strength in compressing the Fe sample. (Figure 8b is adapted with permission from Ref. [63]. Copyrighted by the American Physical Society.)

Figure 9. (a) Schematic of the experimental setup to infer Ta flow stress (strength) at high pressure and high strain rate at the Omega laser facility, using the Rayleigh-Taylor instability.⁸⁵ Radiation from the hohlraum drives the reservoir/gap configuration (not to scale) creating a ramped plasma drive that compresses and accelerates the sample material without shock melting. (Figure 9a is adapted with permission from Ref. [85]. Copyrighted by the American Physical Society.) (b) Time histories of simulation results for laser-driven Rayleigh–Taylor instability growth in the solid-state, plastic flow regime of tantalum, at peak pressures of ~ 100 GPa. The predicted growth factor vs. time for various strength models is shown, as well as an extensive set of experimental data from the Omega laser. (Figure 9b is adapted with permission from Ref. [85]. Copyrighted by the American Physical Society.) (c) Molecular dynamics simulation results (points) and calibrated functional forms (smooth curves) for the mobility of screw dislocations in tantalum at zero pressure. Upper inset: Saturation dislocation density as a function of plastic strain rate for tantalum from dislocation dynamics simulations and a power-law fit to the results.

(Adapted with permission from Ref. 68.) Lower inset: Screw dislocation in Ta under high stress leaving interstitial and vacancy debris in its wake. Only those atoms at defective lattice sites are shown. The dislocation core is the line of red atoms. The colors just indicate position: the dislocation is moving on a glide plane from blue to red (right to left). (Adapted with permission from Ref. 70.) (d) Spatial distribution of quantities in the tantalum for a laser-driven Rayleigh–Taylor instability growth simulation at roughly 50 ns. The other materials in the simulation are not shown. Dislocation density (lower plot) is plotted with a logarithmic scale, and dislocation velocity (upper plot) is on a linear scale. (Adapted with permission from Ref. 68.) (e) A plot of the Ta LMS model flow stress as a function of plastic strain rate at the conditions shown in the plot assuming that the dislocation density is saturated. The LMS model predictions are plotted for the contributions from work hardening and the thermal activation and drag parts of the dislocation mobility. These contributions sum to give the total flow stress, apart from a negligible athermal component. The work hardening contribution is the greatest over the strain rate range 10^6 – 10^8 /s, which includes the strain rate during the RT ripple growth: 3×10^7 /s.⁸⁶ (Adapted with permission from Ref. 86.) (f) Residual dislocation density (horizontal axis) from recovered samples of single crystal Ta shocked along the [100] direction as a function of shock pressure (vertical axis). The inset shows the results from a TEM image for the case of an average shock strength of 22 GPa, and duration of < 50 ns. (Adapted with permission from Ref. 87.)

Figure 10. (a) A schematic representation of the broadband Laue diffraction experiment, showing the 5 μ m Ta sample embedded between polycrystalline diamond layers (10 μ m ablator and 40 μ m tamper) and mounted at the pinhole in the BBXRD diagnostic. A laser beam strikes the ablator, launching a shock in the [100] direction in Ta. 44 laser beams are used to drive a capsule implosion, creating a broadband (“white-light”) x-ray source. The transmission diffraction pattern from the x-rays diffracting off the Ta is depicted on the image plates inside the BBXRD. The locations of the diffraction spots shift as the Ta is shocked and the aspect ratio of the unit cells of the crystal changes. (Figure 10a is adapted with permission from Ref. [88]. Copyrighted by the American Physical Society.) (b) Experimental results for the flow stress of the shocked Ta as a function of the shock pressure, as described in the text. The inset shows the shear modulus used to convert the measured strain to stress. The experimental data are plotted along with the results from the LMS model (MS),⁶⁵ the Preston-Tonks-Wallace model (PTW),⁷² the Steinberg-Lund model (SL) and the Steinberg-Guinan model (SG).^{68,69,71} (Figure 10b is adapted with permission from Ref. [88]. Copyrighted by the American Physical Society.)

Figure 11. (a) Co-axial (left) and stripline (right) load configurations on the SNLA Z high-energy magnetic pinch facility. The coaxial target contains drive measurements on the top and bottom of each anode panel with a sample measurement in between. The stripline target contains three drive measurements on the cathode directly opposed by sample measurements on the anode. (Adapted with permission from Ref. 90.) (b) Ta flow stress τ or yield stress Y from experiments on the Z machine plotted as a function of pressure, along with the results from simulations based on different strength models. Different symbols indicate different batches of material: Starck, Goodfellow, and cold rolled/sputtered. (Adapted with permission from Ref. 90.) A new window response function was used by Brown et al. in a reanalysis of their original data, which shifted their data slightly towards lower inferred shear stress in Fig. 11b here, compared to their original figure in Ref. 90.

Figure 12. (a) Schematic target design to experimentally infer entropy on the principle Hugoniot as a function of temperature for shocked quartz, based on a shock-and-release technique. A quasi-steady shock wave is generated by laser ablation of the aluminized sample. Upon shock breakout at the down-range free surface, the released material propagates across the gap and stagnates against an aluminized LiF window. The particle velocity in the LiF and time of impact were

measured for three gap distances after 199 and 338 GPa shocks in the quartz sample. (Adapted with permission from Ref. 92.) (b) Post-shock temperatures (filled circles) based on streaked optical pyrometry (SOP) measurements for quartz^{89,112} and fused silica¹¹² compared to the revised model liquid-vapor phase boundary from this study. The Hugoniot states achieved in each shock-and-release experiment (open circles) are placed at the entropy and temperature corresponding to the measured shock velocity. Reported uncertainties in entropy reflect both uncertainties in the experimental shock pressure and the absolute entropy on the Hugoniot. (Adapted with permission from Ref. 92.) (c) A decaying blast wave experiment was carried out at the Omega laser, as illustrated in the figure. The planar package corresponded to an ablator of either diamond or beryllium, then a thin gold x-ray preheat shield, followed by an α -quartz reference layer, then the stishovite samples being studied (not shown to scale). (Adapted with permission from Ref. 100.) (d) Plotted are blast wave pressure vs. temperature for a decaying shock launched into the SiO₂ samples being studied. The measured shock temperature curves for fused silica (shaded gray), quartz (shaded red), and stishovite (shaded blue) are plotted as a function of blast wave pressure. The silica melt line is shown in shaded green. The data for gas-gun experiments are given by green circles, red squares, and black triangles. Thick gray lines illustrated the expected solid-phase boundaries. The dotted blue, red, and black curves correspond to calculated Hugoniots below the melt curve for stishovite, quartz, and fused silica. Predictions from simulations using the ANEOS model are shown by the blue dash-dotted curve, and the results from a classical molecular dynamics simulation of the melt curve are given by the dotted green curve. (Adapted with permission from Ref. 100.)

Figure 13. (a) The melting temperature of diamond at high pressures has been experimentally studied at the Omega laser, using a decaying shock (blast wave) technique, with velocity interferometry (VISAR), and time resolved optical pyrometry (SOP).⁹⁹ The experimental configuration is shown (top), followed by a raw VISAR trace, and the analyzed shock velocity vs. time in diamond (bottom). (Adapted with permission from Ref. 99.) (b) The experimentally measured temperature versus pressure data compared with simulations, for the decaying shock in the diamond. The black curve corresponds to the new Omega experimental data. The blue circles and blue dashed curve correspond to the theoretical melt curve from density functional theory.¹⁰⁹ The brown triangles and brown dashed curves represent theoretical calculations by Correa et al.¹¹⁰ (Adapted with permission from Ref. 99.) (c) Velocity interferometry for ramp compressed diamond to ~ 5 TPa (50 Mbar) peak pressures on the NIF laser. The free-surface velocity u_{fs} versus time from the back of the diamond steps obtained from VISAR. The target (inset) consists of a gold cylindrical radiation cavity (hohlraum) within which the 351-nm- wavelength laser light is converted to an x-ray flux that is absorbed by the diamond sample attached to the side of the hohlraum. The x-rays ablate and ramp-compress the sample, and the free-surface velocity is recorded for four thicknesses (steps) of diamond: 140.0 mm (red line), 151.7 mm (blue line), 162.6 mm (black line) and 172.5 mm (green line). (Adapted with permission from Ref. 108.) (d) The free surface velocity vs. time traces through the 4 steps of diamond are analyzed to produce longitudinal stress versus density. Model comparisons include simulated Hugoniots based on density functional theory (DFT) (solid red line) and a Mie–Gruneisen EOS (solid orange line); cold curves from DFT (red dashed line), statistical-atom models (Thomas-Fermi, Thomas-Fermi-Dirac, TFD-W and TFD-Wc as green dotted, short dashed, long dashed and solid lines), and Vinet (gray dot-dashed line) and Birch–Murnaghan (grey dashed line) EOS fits to static data. Static diamond anvil cell (DAC) data are shown as the green circles in the lower left corner. Shaded regions between cold curves (gray) or Hugoniot curves (orange) show roughly the range of uncertainty in the EOS in this terapascal regime. The pressures at the center of Earth, Neptune and Saturn are shown with red arrows along the vertical axis for reference. The inset highlights the differences in the models at low pressure. (Adapted with permission from Ref. 108.)

Fig. 14. (a) Schematic of the experimental setup for radiography measurements of EOS at near-Gbar pressures. Here solid targets of CH, CD, or diamond (carbon) are shock compressed using a hohlraum radiation source. The plasma is probed with x-ray radiography in the horizontal direction and x-ray scattering in the polar direction. The inset at the upper left shows a wedged cross-section of the solid CH target with a Ge doped CH ablator. Shown on the left hand side are the radii of the layers, and on the right hand side are the percent dopant of the Ge layers. (Adapted with permission from Ref. 113.) (b) Pressure as a function of shock radius for simulations using various equation of state models: LEOS 5350 (red), LEOS 5400 (green), and Sesame 7592 (black). Inset: Simulated radiograph of an imploding solid CH sphere, with a noise function derived from previous shots. Also plotted is the location of the predicted self-emission flash. Fiducial wires are used to determine the magnification of the instrument and a 4ω fiducial is used to determine the absolute diagnostic timing. (Adapted with permission from Ref. 113.)

Fig. 15. (a) Schematic of the experimental setup. The laser (energy of 65 J, 11 ns pulse duration, $1.064\ \mu\text{m}$ wavelength, $250\ \mu\text{m}$ spot size) is incident from the right onto the graphite sample, launching a shock that compresses and heats the carbon sample. Another laser (energy of 150 J, 1 ns pulse duration, $0.527\ \mu\text{m}$ wavelength, $70\ \mu\text{m}$ spot size) irradiates a titanium foil to generate Ti helium-alpha radiation at 4.75 keV which is collimated by a pinhole for backlighting the shocked graphite sample. The scattered radiation is recorded with two spectrally resolved HOPG spectrometers located at angles of 105° and 126° , relative to the direction of the shock velocity in the graphite. [Figure 15a is adapted with permission from Ref. [118]. Copyrighted by the American Physical Society.] (b) An example x-ray scattering spectrum from the HOPG spectrometer located at 126° . The dashed green curve corresponds to the elastic feature, and the dot-dashed red curve represents the inelastic feature. The sum is the solid blue curve. [Figure 15b is adapted with permission from Ref. [118]. Copyrighted by the American Physical Society.] (c) Comparison of the experimentally measured ion-ion density correlation function, $S_{ii}(k)$, also called the atomic structure factor, with *ab initio* DFT-MD simulations of the shocked carbon in various phases, and at various densities and temperatures. Carbon phases considered are cubic diamond, hexagonal diamond, or liquid carbon. For reference, the Bragg maxima of the crystalline solid phases are indicated by short lines at the top and bottom. For the low-pressure case, additional theoretical comparisons are made corresponding to MD simulations using a hypernetted chain (HNC) Lennard-Jones (LJ) potential, and a more complex LCBOP potential. [Figure 15c is adapted with permission from Ref. [118]. Copyrighted by the American Physical Society.]

Acknowledgements:

*This work performed under the auspices of the U.S. Department of Energy by Lawrence Livermore National Laboratory under Contract DE-AC52-07NA27344.

We thank Justin L. Brown from SNLA for providing a updated results for Fig. 11b, prior to publication. A new window response function was used in their data analysis, which shifted their data slightly towards lower inferred shear stress.

References:

¹B.A. Buffett, [Science](#) 288, 2007 (2000).

- ²A. M. Dziewonski and D. L. Anderson, [Phys. Earth Planet. Inter.](#) 25, 297 (1981).
- ³Jue Wang, Raymond F. Smith, Jon H. Eggert, Dave G. Braun, Thomas R. Boehly, J. Reed Patterson, Peter M. Celliers, Raymond Jeanloz, Gilbert W. Collins, and Thomas S. Duffy, *J. Appl. Phys.* 114, 023513 (2013).
- ⁴Seager, S., Kuchner, M., Hier-Majumder, C. A. & Militzer, B. Mass-radius relationships for solid exoplanets. *Astrophys. J.* 669, 1279–1297 (2007). (2002).
- ⁵Schneider, J., Dedieu, C., Le Sidaner, P., Savalle, R. & Zolotukhin, I. Defining and cataloging exoplanets: the exoplanet.eu database. *Astron. Astrophys.* 532, A79 (2011).
- ⁶D. Valencia, R. J. O’Connell, and D. Sasselov, *Icarus* 181, 545 (2006).
- ⁷D. Valencia, R. O’Connell, and D. Sasselov, *Astrophys. Space Sci.* 322, 135 (2009).
- ⁸D. C. Swift, J. H. Eggert, D. G. Hicks, S. Hamel, K. Caspersen, E. Schwegler, G. W. Collins, N. Nettelmann, and G. J. Ackland, *Astrophys. J.* 744, 59 (2012).
- ⁹J. J. Fortney, S. H. Glenzer, M. Koenig, B. Militzer, D. Saumon, and D. Valencia, *Phys. Plasmas* 16, 041003 (2009).
- ¹⁰C. Sotin, O. Grasset, and A. Mocquet, *Icarus* 191, 337 (2007).
- ¹¹S. W. Haan, J. D. Lindl, D. A. Callahan, D. S. Clark, J. D. Salmonson, B. A. Hammel, L. J. Atherton, R. C. Cook, M. J. Edwards, S. Glenzer,, *Phys. Plasmas* 18, 051001 (2011).
- ¹²M. J. Edwards, J. D. Lindl, B. K. Spears, S. V. Weber, L. J. Atherton, D. L. Bleuel, D. K. Bradley, D. A. Callahan, C. J. Cerjan, D Clark et al., *Phys. Plasmas* 18, 051003 (2011).
- ¹³M. J. Edwards, P. K. Patel, J. D. Lindl, L. J. Atherton, S. H. Glenzer, S. W. Haan, J. D. Kilkenny, O. L. Landen, E. I. Moses, A. Nikroo, *Phys. Plasmas* 20, 070501 (2013).
- ¹⁴Mordecai D. Rosen, *Phys. Plasmas* 3, 1803 (1996).
- ¹⁵Mordecai D. Rosen, *Phys. Plasmas* 6, 1690 (1999).
- ¹⁶D. Rosen et al., *Phys. Plasmas*, in prep. (2015).
- ¹⁷Bruce A. Remington, David Arnett, R. Paul Drake, Hideaki Takabe, *Science* 284, 1488 (1999).
- ¹⁸Bruce A. Remington, R. Paul Drake, Hideaki Takabe, David Arnett, *Phys. Plasmas* 7, 1641 (2000).
- ¹⁹Bruce A. Remington, R. Paul Drake, and Dmitri D. Ryutov, *Rev. Mod. Phys.* 78, 755 (2006).

- ²⁰Leonid Dubrovinsky, Natalia Dubrovinskaia, Vitali B. Prakapenka, and Artem M. Abakumov, *Nat. Commun.* 3, 1163 (2012).
- ²¹R.E. Rudd, T.C. Germann, B.A. Remington, and J.S. Wark, *MRS Bulletin* 35, 999 (2010).
- ²²L.M. Barker and R.E. Hollenbach, *JAP* 45, 4872 (1974).
- ²³Dennison Bancroft, Eric L. Peterson, and Stenley Minshall, *J. Appl. Phys.* 27, 291 (1956).
- ²⁴R.F. Smith, J. H. Eggert, D. C. Swift, J. Wang, T. S. Duffy, D. G. Braun, R. E. Rudd, D. B. Reisman, J.-P. Davis, M. D. Knudson, and G. W. Collins, *J. Appl. Phys.* 114, 223507 (2013).
- ²⁵M. Keith Matzen, M. A. Sweeney, R. G. Adams, J. R. Asay, J. E. Bailey, G. R. Bennett, D. E. Bliss, D. D. Bloomquist, T. A. Brunner, R. B. Campbell, *Phys. Plasmas* 12, 055503 (2005).
- ²⁶Tatsuhiko Sakaiya, Hideki Takahashi, Tadashi Kondo, Toshihiko Kadono, Yoichiro Hironaka, Tetsuo Irifune, Keisuke Shigemori, *Earth Planet. Sci. Lett.* 392, 80 (2014).
- ²⁷K. Shigemori, T. Sakaiya, Y. Asakura, T. Kondo, K. Shimizu, T. Kadono, Y. Hironaka, and H. Azechi, *Rev. Sci. Instrum.* 83, 10E529 (2012).
- ²⁸N. Amadou, E. Brambrink, T. Vinci, A. Benuzzi-Mounaix, G. Huser, S. Brygoo, G. Morard, F. Guyot, T. de Resseguier, S. Mazevet, K. Miyaniishi, N. Ozaki, R. Kodama, O. Henry, D. Raffestin, T. Boehly, and M. Koenig, *Phys. Plasmas* 22, 022705 (2015).
- ²⁹Justin S. Wark, Robert R. Whitlock, Allan A. Hauer, James E. Swain, and Paul J. Solone., *Phys. Rev. B* 40, 5705 (1989).
- ³⁰T. R. Boehly, D.L. Brown, R.S. Craxton, R.L. Keck, J.P. Knauer, J.H. Kelly, T.J. Kessler, S.A. Kumpan, S.J. Loucks, S.A. Letzring, F.J. Marshall, R.L. McCrory, S.F.B. Morse, W. Seka, J.M. Soures, and C.P. Verdon, *Opt. Commun.* **133**, 495 (1997).
- ³¹Jonathan C. Crowhurst, Michael R. Armstrong, Kimberly B. Knight, Joseph M. Zaug, and Elaine M. Behymer, *Phys. Rev. Lett.*, 107, 144302 (2011); Jonathan C. Crowhurst, Ryan W. Reed, Michael R. Armstrong, Harry B. Radousky, Jeffrey A. Carter, Damian C. Swift, Joseph M. Zaug, Roger W. Minich, Nick E. Teslich, and Mukul Kumar, *J. Appl. Phys.* 115, 113506 (2014).
- ³²J.S. Wark, R.R. Whitlock, A. Hauer, J.E. Swain, and P.J. Solone, *Phys. Rev. B., Rapid Commun.*, 35, 9391 (1987).
- ³³A. Loveridge-Smith, A. Allen, J. Belak, T. Boehly, A. Hauer, B. Holian, D. Kalantar, G. Kyrala, R. W. Lee, P. Lomdahl, M. A. Meyers, D. Paisley, S. Pollaine, B. Remington, D. C. Swift, S. Weber, and J. S. Wark, *Phys. Rev. Lett.* 86, 2349 (2001)
- ³⁴G. Mogni, A. Higginbotham, K. Gaál-Nagy, N. Park, and J.S. Wark, *Phys. Rev. B* 89, 064104 (2014).
- ³⁵B.L. Holian and P.S. Lomdahl, *Science* 280, 2085 (1998).
- ³⁶Rosolankova, K.; Kalantar, D.H.; Belak, J.F.; Bringa, E.M.; Caturla, M.J.; Hawreliak, J.; Holian, B.L.; Kadau, K.; Lomdahl, P.S.; Germann, T.C.; Ravelo, R.; Sheppard, J.; Wark, J.S. et al., in

“Shock Compression of Condensed Matter-2003” (eds. M.D. Furnish, Y.M. Gupta and J.W. Forbes) 1195 (AIP, Melville, New York, 2004).

³⁷E.M. Bringa, K. Rosolankova, R. E. Rudd, B. A. Remington, J. S. Wark, M. Duchaineau, D. H. Kalantar, J. Hawreliak and J. Belak, *Nature Materials* 5, 805 (2006).

³⁸Y. Mishin, M. J. Mehl and D. A. Papaconstantopoulos, A. F. Voter and J. D. Kress, *Phys. Rev. B* 63, 224106–224121 (2001).

³⁹D. Milathianaki, S. Boutet, G. J. Williams, A. Higginbotham, D. Ratner, A. E. Gleason, M. Messerschmidt, M. M. Seibert, D. C. Swift, P. Hering, J. Robinson, W. E. White, J. S. Wark, *Science* 342, 220 (2013).

⁴⁰Virginie Dupont and Timothy C. Germann, *PRB* 86, 134111 (2012).

⁴¹D.H. Kalantar, J. F. Belak, G. W. Collins, J. D. Colvin, H. M. Davies, J. H. Eggert, T. C. Germann, J. Hawreliak, B. L. Holian, K. Kadau, P. S. Lomdahl, H. E. Lorenzana, M. A. Meyers, K. Rosolankova, M. S. Schneider, J. Sheppard, J. S. Stolken, and J. S. Wark, *Phys. Rev. Lett.* 95, 075502 (2005).

⁴²J. Hawreliak, J. D. Colvin, J. H. Eggert, D. H. Kalantar, H. E. Lorenzana, and J. S. Stölken, H. M. Davies, T. C. Germann, B. L. Holian, K. Kadau, and P. S. Lomdahl, A. Higginbotham, K. Rosolankova, J. Sheppard, and J. S. Wark, *PRB* 74, 184107 (2006).

⁴³Justin Wark, Andrew Higginbotham, Giles Kimminau, William Murphy, Bob Nagler, Thomas Whitcher, James Hawreliak, Dan Kalantar, Martin Butterfield, Bassem El-Dasher, James McNaney, Despina Milathianaki, Hector Lorenzana, Bruce Remington, Huw Davies, Lee Thornton, Nigel Park and Stan Lukezic, *Proc. SCCM-07*, p.286 (2007).

⁴⁴Kai Kadau, Timothy C. Germann, Peter S. Lomdahl, and Brad Lee Holian, *Science* **296**, 1681 (2002).

⁴⁵Kai Kadau, Timothy C. Germann, Peter S. Lomdahl, and Brad Lee Holian, *Phys. Rev. B* 72, 064120 (2005).

⁴⁶J. Hawreliak, Daniel H. Kalantar, James S. Stölken, Bruce A. Remington, and Hector E. Lorenzana, Justin S. Wark, *PRB* 78, 22010 (R) (2008).

⁴⁷J. Hawreliak, Bassem El-Dasher, and Hector Lorenzana, Giles Kimminau, Andrew Higginbotham, Bob Nagler, Sam M. Vinko, William J. Murphy, Thomas Whitcher, and Justin S. Wark, Steve Rothman and Nigel Park, *Phys. Rev. B* 83, 144114 (2011).

⁴⁸Kai Kadau, Timothy C. Germann, Peter S. Lomdahl, Robert C. Albers, Justin S. Wark, Andrew Higginbotham, and Brad Lee Holian, *Phys. Rev. Lett.* 98, 135701 (2007).

⁴⁹Thomas S. Duffy, Russell J. Hemley, and ho-kwang Mao, *Phys. Rev. Lett.* 74, 1371 (1995).

⁵⁰Koichiro Umemoto, Renata M. Wentzcovitch, Philip B. Allen, *Science* 311, 983 (2006).

⁵¹R. Stewart McWilliams, Dylan K. Spaulding, Jon H. Eggert, Peter M. Celliers, Damien G. Hicks, Raymond F. Smith, Gilbert W. Collins, Raymond Jeanloz, *Science* 338, 1330 (2012).

- ⁵²F. Coppari, R. F. Smith, J. H. Eggert, J. Wang, J. R. Rygg, A. Lazicki, J. A. Hawreliak, G. W. Collins and T. S. Duffy, *Nature Geoscience* **6**, 926 (2013).
- ⁵³D.C. Konningsberger and R. Prins, *X-ray Absorption: Principles, Applications, Techniques of EXAFS, SEXAFS, and XANES* (John Wiley & Sons, 1988).
- ⁵⁴P.A. Lee, P.H. Citrin, P. Eisenberger, and B.M. Kincaid, *Rev. Mod. Phys.* **53**, 769 (1981).
- ⁵⁵B. Yaakobi, F. J. Marshall, T. R. Boehly, R. P. J. Town, and D. D. Meyerhofer, *J. Optical Soc. America B-Optical Physics* **20**, 238 (2003).
- ⁵⁶B. Yaakobi, D. D. Meyerhofer, and T. R. Boehly, J. J. Rehr, B. A. Remington, P. G. Allen, and S. M. Pollaine, R.C. Albers, *PRL* **92**, 095504 (2004).
- ⁵⁷B. Yaakobi, D. D. Meyerhofer, and T. R. Boehly, J. J. Rehr, B. A. Remington, P. G. Allen, and S. M. Pollaine, R. C. Albers, *PoP* **11**, 2688 (2004).
- ⁵⁸J. Rehr and R.C. Albers, *Rev. Mod. Phys.* **72**, 621 (2000).
- ⁵⁹Yang Ding, Rajeev Ahuja, Jinfu Shu, Paul Chow, Wei Luo, and Ho-kwang Mao, *Phys. Rev. Lett.* **98**, 085502 (2007).
- ⁶⁰G B. Zimmerman and W. L. Kruer, *Comments Plasma Phys. Controlled Fusion* **2**, 51 (1975).
- ⁶¹B. Yaakobi, T. R. Boehly, D. D. Meyerhofer, and T. J. B. Collins, B. A. Remington, P. G. Allen, S. M. Pollaine, H. E. Lorenzana, and J. H. Eggert, *Phys. Rev. Lett.* **95**, 075501 (2005).
- ⁶²B. Yaakobi, T. R. Boehly, D. D. Meyerhofer, and T. J. B. Collins, B. A. Remington, P. G. Allen, S. M. Pollaine, H. E. Lorenzana, and J. H. Eggert, *Phys. Plasmas* **12**, 092703 (2005).
- ⁶³Yuan Ping, F. Coppari, D. G. Hicks, B. Yaakobi, D. E. Fratanduono, S. Hamel, J. H. Eggert, J. R. Rygg, R. F. Smith, D. C. Swift, D. G. Braun, T. R. Boehly, and G. W. Collins, *PRL* **111**, 065501 (2013).
- ⁶⁴Andrea Di Cicco, Mario Berrettoni, and Sergio Stizza, Ennio Bonetti, Giorgio Cocco, ., *Phys. Rev. B* **50**, 12386 (1994).
- ⁶⁵X. Zhu, R. Birringer, U. Herr, and H. Gleiter, *Phys. Rev. B* **35**, 9085 (1987).
- ⁶⁶Andrew Higginbotham, Robert C. Albers, Timothy C. Germann, Brad Lee Holian, Kai Kadau, Peter S. Lomdahl, William J. Murphy, Bob Nagler, Justin S. Wark, *High Energy Density Phys.* **5**, 44 (2009).
- ⁶⁷Russell J. Hemley, Ho-kwang Mao, Guoyin Shen,† James Badro, Philippe Gillet, Michael Hanfland, Daniel Hausermann, *Science* **276**, 1242 (1997).
- ⁶⁸N.R. Barton, J. V. Bernier, R. Becker, A. Arsenlis, R. Cavallo, J. Marian, M. Rhee, H.-S. Park, B. A. Remington, and R. T. Olson, *J. Appl. Phys.* **109**, 073501 (2011); Nathan Barton and Moon Rhee, *JAP* **114**, 123507 (2013).

- ⁶⁹R. E. Rudd, A. J. Comley, J. Hawreliak, B. Maddox, H.-S. Park, B. A. Remington, in *Shock Compression of Condensed Matter— 2011*, edited by M. L. Elert, W. T. Buttler, J. P. Borg, J. L. Jordan, and T. J. Vogler (American Institute of Physics, Melville, 2012), Vol. 1426, p. 1379.
- ⁷⁰R.E. Rudd, A Arsenlis, N R Barton, R M Cavallo, A J Comley, B R Maddox, J Marian, H-S Park, S T Prsbrey, C E Wehrenberg, L Zepeda-Ruiz and B A Remington, *J. Phys. Conf. Ser.* 500, 112055 (2014).
- ⁷¹B.A. Remington, G. Bazan, J. Belak, E. Bringa, M. Caturla, J.D. Colvin, M.J. Edwards, S.G. Glendinning, D.S. Ivanov, B.Kkad, D.H. Kalantar, M. Kumar, B.F. Lasinski, K.T. Lorenz, J.M. McNaney, D.D. Meyerhofer, M.A. Meyers, S.M. Pollaine, D. Rowley, M. Schneider, J.S. Stölken, J.S. Wark, S.V. Weber, W.G. Wolfer, B. Yaakobi, and L.V. Zhigilei, *Met. Mat. Trans. A* 35A, 2587 (2004).
- ⁷²B.A. Remington, P. Allen, E. M. Bringa, J. Hawreliak, D. Ho, K. T. Lorenz, H. Lorenzana, J. M. McNaney, M. A. Meyers, S. W. Pollaine, K. Rosolankova, B. Sadik, M. S. Schneider, D. Swift, J. Wark and B. Yaakobi, *Mat Sci. Tech.* 22, 474 (2006).
- ⁷³D. J. Steinberg, S. G. Cochran, and M. W. Guinan, *J. Appl. Phys.* **51**, 1498 (1980).
- ⁷⁴D.J. Steinberg and C.M. Lund, *J. Appl. Phys.*, vol. 65, p. 1528 (1989).
- ⁷⁵D. L. Preston, D. L. Tonks, and D. C. Wallace, *J. Appl. Phys.* **93**, 211 (2003).
- ⁷⁶John F. Barnes, Patrick J. Blewett, Robert G. McQueen, Kenneth A. Meyer, and Douglas Venable, *J. Appl. Phys.* 45, 727 (1974).
- ⁷⁷J.D. Colvin, M. Legrand, B.A. Remington, G. Schurtz, and S.V. Weber, *J. Appl. Phys.* 93, 5287 (2003).
- ⁷⁸A.C. Robinson and J.W. Swegle, *J. Appl. Phys.* 66, 2859 (1989).
- ⁷⁹J.W. Swegle and A.C. Robinson, *J. Appl. Phys.* 66, 2838 (1989).
- ⁸⁰T. Ma, P. K. Patel, N. Izumi, P. T. Springer, M. H. Key, L. J. Atherton, L. R. Benedetti, D. K. Bradley, D. A. Callahan, P. M. Celliers, *Phys. Rev. Lett.* 111, 085004 (2013).
- ⁸¹Shuh Rong Chen and George T. Gray III, *Met. Mat. Trans. A* 27A, 2994 (1996).
- ⁸²Hye-Sook Park, K. T. Lorenz, R. M. Cavallo, S. M. Pollaine, S. T. Prsbrey, R. E. Rudd, R. C. Becker, J. V. Bernier, and B. A. Remington, *Phys. Rev. Lett.* 104, 135504 (2010).
- ⁸³H.-S. Park, B. A. Remington, R. C. Becker, J. V. Bernier, R. M. Cavallo, K. T. Lorenz, S. M. Pollaine, S. T. Prsbrey, R. E. Rudd, and N. R. Barton, *Phys. Plasmas* **17**, 056314 (2010).
- ⁸⁴H. S. Park, N. R. Barton, J. L. Belof, K. J. M. Blobaum, R. M. Cavallo, A. J. Comley, B. R. Maddox, M. J. May, S. M. Pollaine, S. T. Prsbrey, B. A. Remington, R. E. Rudd, D. W. Swift, R. J. Wallace, M. J. Wilson, A. Nikroo, and E. Giraldez, in *Shock Compression of Condensed Matter— 2011*, edited by M. L. Elert, W. T. Buttler, J. P. Borg, J. L. Jordan, and T. J. Vogler (American Institute of Physics, Melville, 2012), Vol. 1426, p. 1371.

- ⁸⁵H. -S. Park and R. E. Rudd, R. M. Cavallo, N. R. Barton, A. Arsenlis, J. L. Belof, K. J. M. Blobaum, B. S. El-dasher, J. N. Florando, C. M. Huntington, B. R. Maddox, M. J. May, C. Plechaty, S. T. Prisbrey, B. A. Remington, R. J. Wallace, C. E. Wehrenberg and M. J. Wilson, A. J. Comley, E. Giraldez, A. Nikroo, M. Farrell, G. Randall, and G. T. Gray III, *Phys. Rev. Lett.*, **114**, 065502 (2015).
- ⁸⁶B.A. Remington, R. E. Rudd, N. R. Barton, R. M. Cavallo, Hye-Sook Park, J. Belof, A. J. Comley, B. R. Maddox, M. J. May, S. M. Pollaine, and S. T. Prisbrey, in *Shock Compression of Condensed Matter—2011*, edited by M. L. Elert, W. T. Buttler, J. P. Borg, J. L. Jordan, and T. J. Vogler (American Institute of Physics, Melville, 2012), Vol. 1426, p. 1375.
- ⁸⁷C.H. Lu, B.A. Remington, B.R. Maddox, B. Kad, H.S. Park, S.T. Prisbrey, and M.A. Meyers, *Acta Mat.* **60**, 6601 (2012).
- ⁸⁸A. J. Comley, B. R. Maddox, R. E. Rudd, S. T. Prisbrey, J. A. Hawreliak, D. A. Orlikowski, S. C. Peterson, J. H. Satcher, A. J. Elsholz, H.-S. Park, B. A. Remington, N. Bazin, J. M. Foster, P. Graham, N. Park, P. A. Rosen, S. R. Rothman, A. Higginbotham, M. Suggit, and J. S. Wark, *Phys. Rev. Lett.* **110**, 115501 (2013).
- ⁸⁹J. R. Asay, T. Ao, T. J. Vogler, J. P. Davis, and G. T. Gray, *J. Appl. Phys.* **106**, 073515 (2009).
- ⁹⁰J.L. Brown, C. S. Alexander, J. R. Asay, T. J. Vogler, D. H. Dolan, and J. L. Belof, *JAP* **115**, 043530 (2014).
- ⁹¹J.R. Asay and J. Lipkin, *JAP* **49**, 4242 (1978).
- ⁹²R. G. Kraus, S. T. Stewart, D. C. Swift, C. A. Bolme, R. F. Smith, S. Hamel, B. D. Hammel, D. K. Spaulding, D. G. Hicks, J. H. Eggert, and G. W. Collins, *J. Geophys. Res.* **117**, E09009 (2012).
- ⁹³Sarah T. Stewart and Zoe M. Leinhardt, *Astrophys. J.* **751**, 32 (2012).
- ⁹⁴Benz, W., W. L. Slattery, and A. G. W. Cameron, *Icarus*, **74**(3), 516–528 (1988).
- ⁹⁵Benz, W., A. Anic, J. Horner, and J. A. Whitby, *Solar Syst. Rev.*, **132**, 189–202 (2007).
- ⁹⁶Canup, R. M., and E. Asphaug, *Nature*, **412**, 708 (2001).
- ⁹⁷Canup, R. M., *Science* **307**, 546–550 (2005).
- ⁹⁸Ahrens, T. J., and J. D. O’Keefe, *Moon*, **4**(1–2), 214–249 (1972).
- ⁹⁹J.H. Eggert, D. G. Hicks, P. M. Celliers, D. K. Bradley, R. S. McWilliams, R. Jeanloz, J. E. Miller, T. R. Boehly and G. W. Collins, *Nature Physics* **6**, 40 (2010).
- ¹⁰⁰M. Millot, N. Dubrovinskaia, A. Černok, S. Blaha, L. Dubrovinsky, D. G. Braun, P. M. Celliers, G. W. Collins, J. H. Eggert, R. Jeanloz, *Science* **347**, 418 (2015).
- ¹⁰¹T. Guillot, *Annu. Rev. Earth Planet. Sci.* **33**, 493–530 (2005).
- ¹⁰²Joe M. Leinhardt and Sarah T. Stewart, *Ap. J.* **745**, 79 (2012).

- ¹⁰³Robin M. Canup, *Science* 338, 1052 (2012).
- ¹⁰⁴Geoffrey F. Davies, *Geophys. Res. Lett.* 9, 1267 (1982).
- ¹⁰⁵V.V. Shuvalov, N.A. Artemeva, and I.B. Kosarev, *Int'l J. Imp. Eng.* 23, 847 (1999).
- ¹⁰⁶V.V. Shuvalov and N.A. Artemieva, *Planet. Space Sci.* 50, 181 (2002).
- ¹⁰⁷N.V. Vasilyev, *Planet. Space Sci.* 46, 129 (1998).
- ¹⁰⁸R.F. Smith, J. H. Eggert, R. Jeanloz, T. S. Duffy, D. G. Braun, J. R. Patterson, R. E. Rudd, J. Biener, A. E. Lazicki, A. V. Hamza, J. Wang, T. Braun, L. X. Benedict, P. M. Celliers, and G. W. Collins, *Nature* 511, 330 (2014).
- ¹⁰⁹Xiaofei Wang, Sandro Scandolo, and Roberto Car, *Phys. Rev. Lett.* 95, 185701 (2005).
- ¹¹⁰Alfredo A. Correa, Stanimir A. Bonev, and Giulia Galli, *Proc. Natl. Acad. Sci. USA* 103, 1204–1208 (2006).
- ¹¹¹Rothman, S. D., J-P Davis, J Maw, C M Robinson, K Parker and J Palmer, *J. Phys. D* 38, 733–740 (2005).
- ¹¹²A.L. Kritcher, T. Döppner, C. Fortmann, T. Ma, O. L. Landen, R. Wallace, and S. H. Glenzer, *Phys. Rev. Lett.* 107, 015002 (2011).
- ¹¹³A.L. Kritcher, T. Döppner, D. Swift, J. Hawreliak, G. Collins, J. Nilsen, B. Bachmann, E. Dewald, D. Strozzi, S. Felker, O.L. Landen, O. Jones, C. Thomas, J. Hammer, C. Keane, H.J. Lee, S.H. Glenzer, S. Rothman, D. Chapman, D. Kraus, P. Neumayer, R.W. Falcone, *HEDP* 10, 27 (2014).
- ¹¹⁴B. Svendsen, T. J. Ahrens, *Geophys. J. R. Astron. Soc.* 91, 667 (1987).
- ¹¹⁵Boslough, M. B., *J. Geophys. Res.*, 93, 6477–6484 (1988).
- ¹¹⁶T. Döppner, A. L. Kritcher, P. Neumayer, D. Kraus, B. Bachmann, S. Burns, R. W. Falcone, S. H. Glenzer, J. Hawreliak, A. House, O. L. Landen, S. LePape, T. Ma, A. Pak, and D. Swift, *Rev. Sci. Instrum.* 85, 11D617 (2014).
- ¹¹⁷G. Schaumann, S.S. Schollmeier, S. Rodriguez-Prieto, A. Blazevic, E. Brambrink, M. Geissel, S. Korostiy, P. Pirzadeh, M. Roth, F. B. Rosmej, A.Ya. Faenov, T.A. Pikuz, K. Tsigutkin, Y. Maron, N.A. Tahir, and D.H.H. Hoffmann, *Laser Part. Beams* 23, 503 (2005).
- ¹¹⁸D. Kraus, J. Vorberger, D. O. Gericke, V. Bagnoud, A. Blazevic, W. Cayzac, A. Frank, G. Gregori, A. Ortner, A. Otten, F. Roth, G. Schaumann, D. Schumacher, K. Siegenthaler, F. Wagner, K. Wu'nsch, and M. Roth, *Phys. Rev. Lett.* 111, 255501 (2013).
- ¹¹⁹G. Gregori, S. H. Glenzer, W. Rozmus, R. W. Lee, and O. L. Landen, *Phys. Rev. E* 67, 026412 (2003).

¹²⁰Raymond Jeanloz, Peter M. Celliers, Gilbert W. Collins, Jon H. Eggert, Kanani K. M. Lee, R. Stewart McWilliams*, Stephanie Brygoo, and Paul Loubeyre, Proc. Nat. Academy Sciences 104, 9172 (2007).

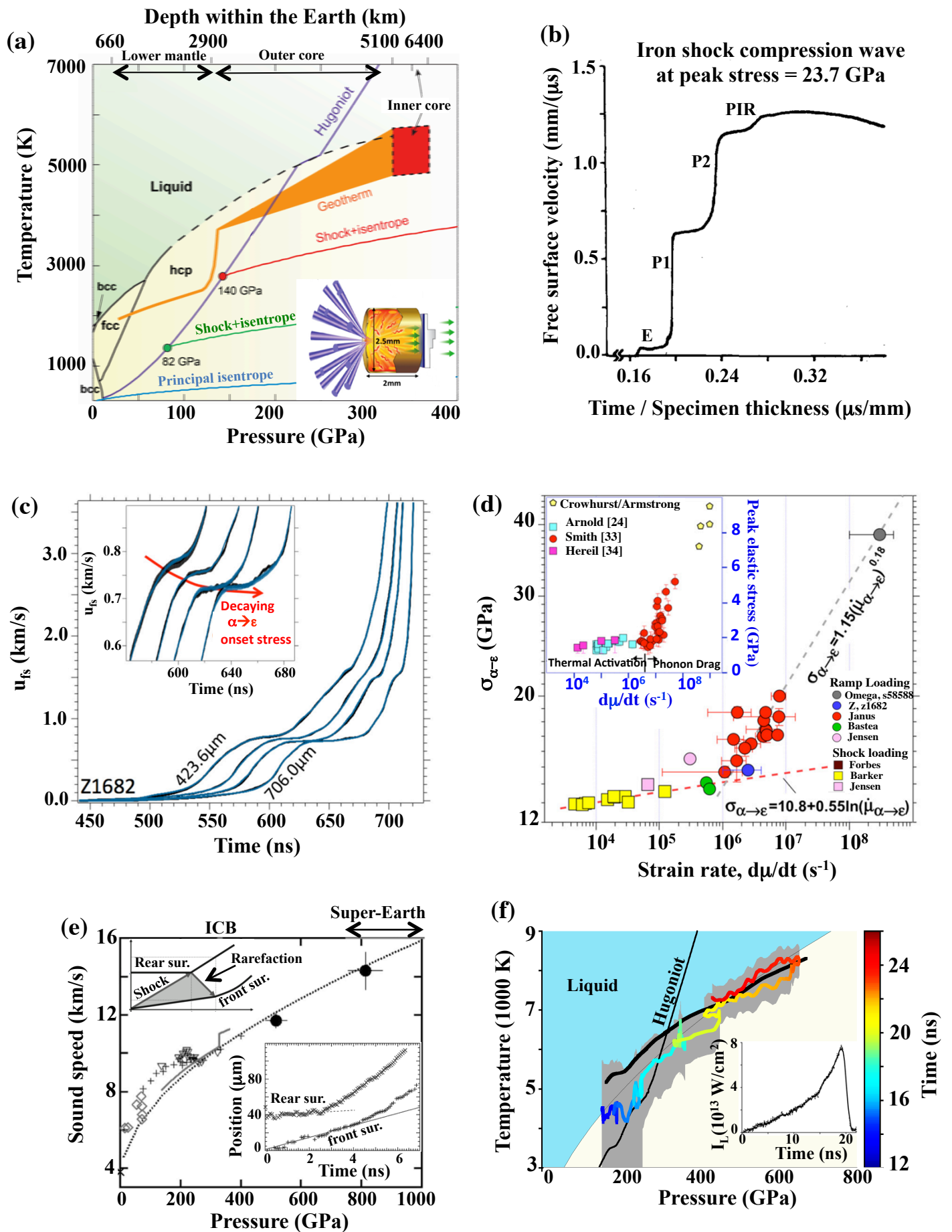


Figure 1

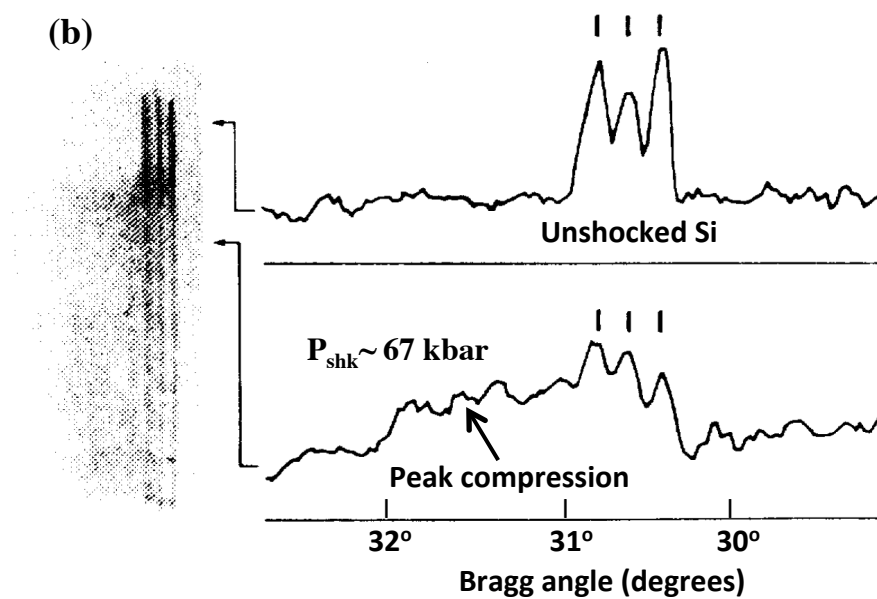
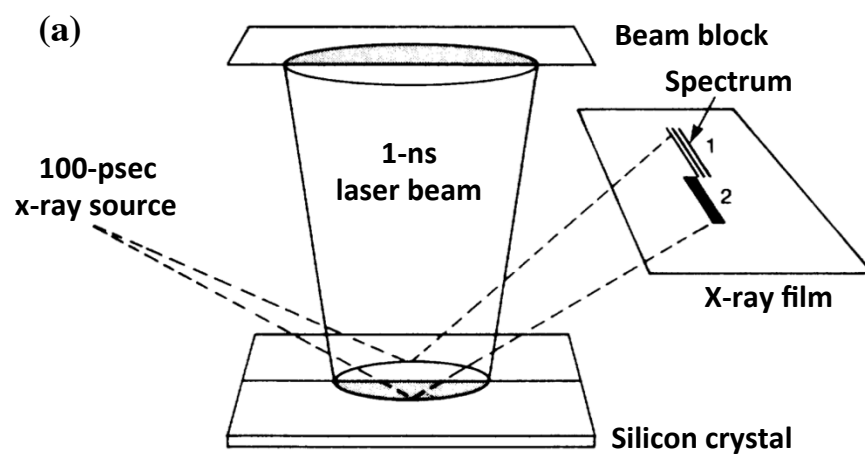


Figure 2

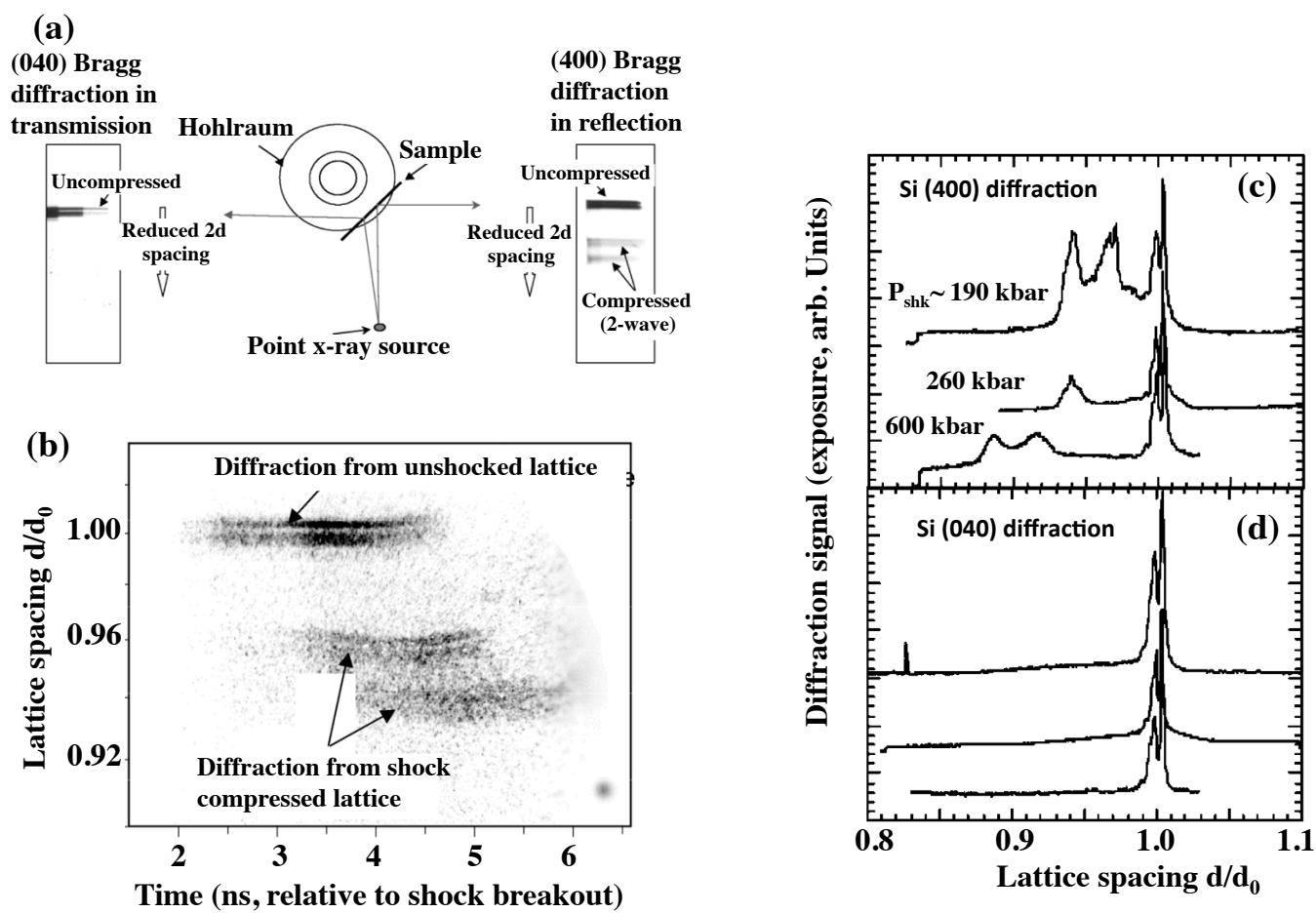


Figure 3

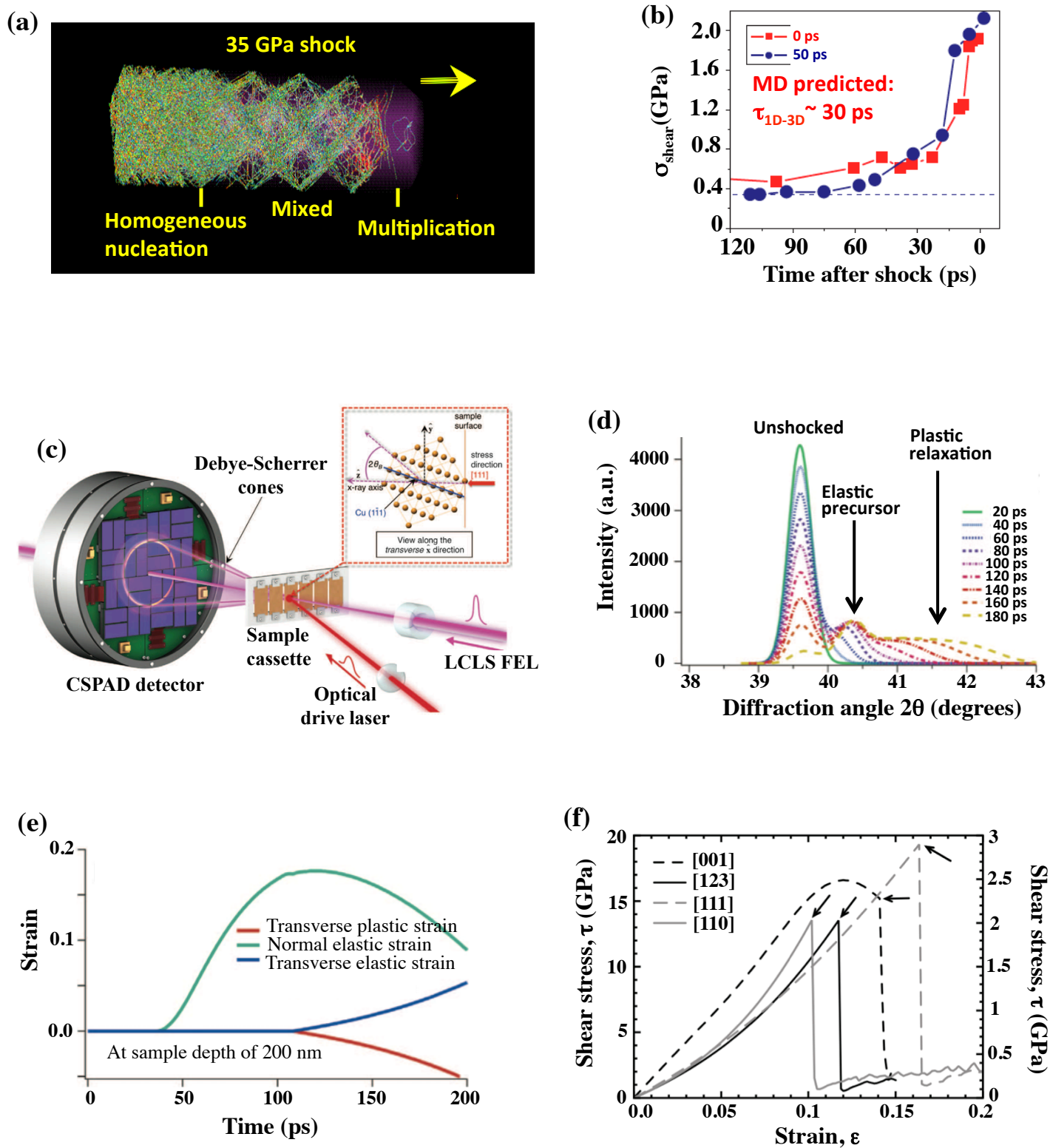


Figure 4

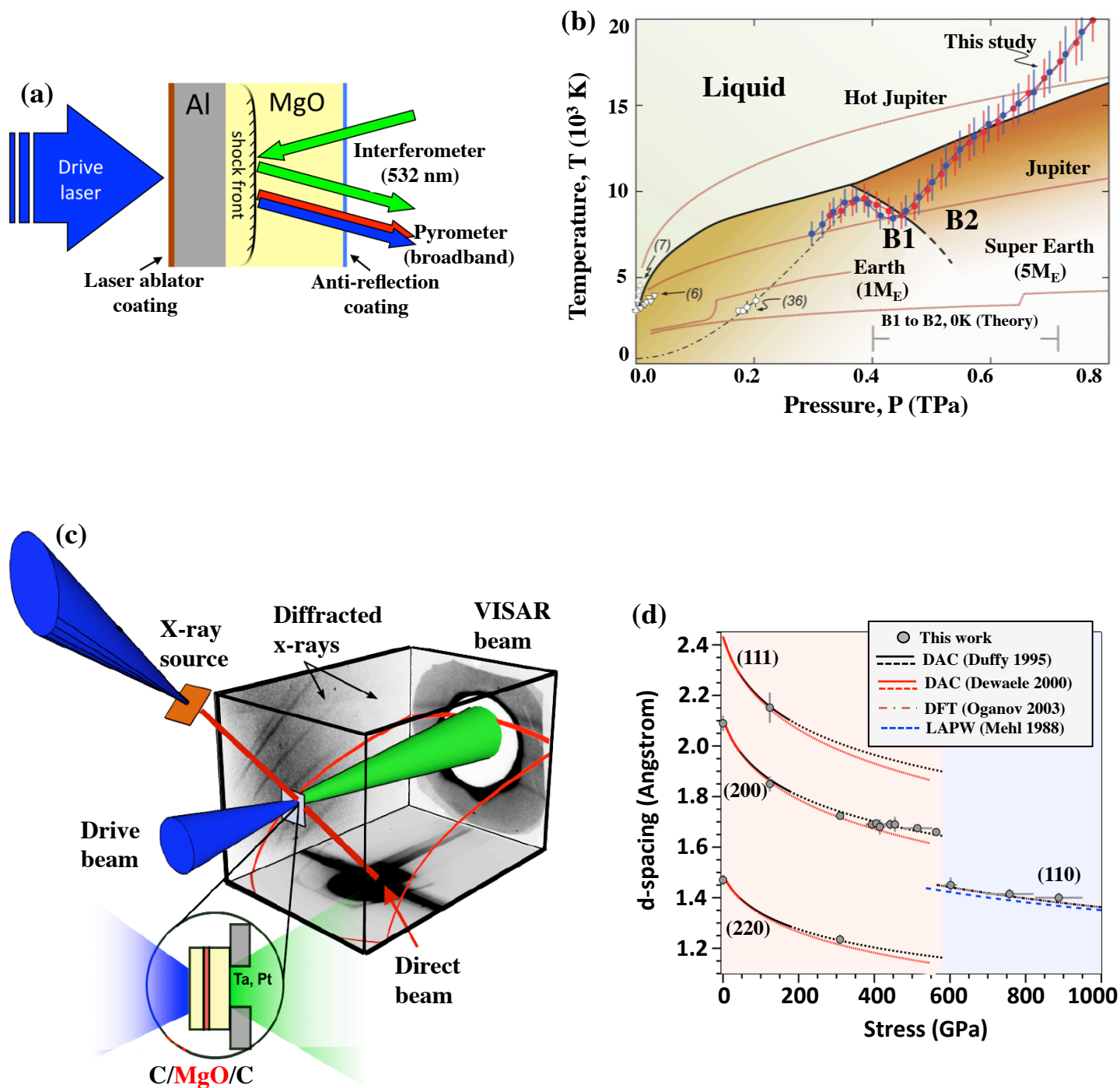


Figure 6

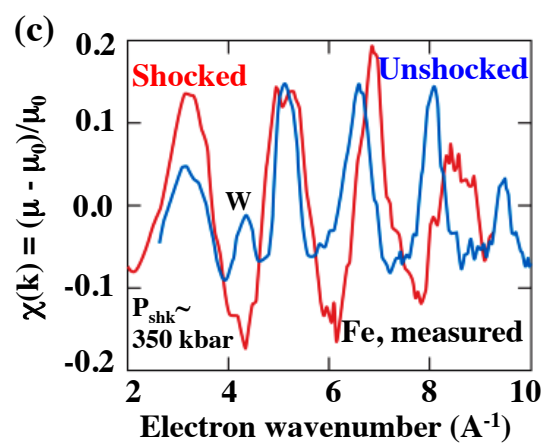
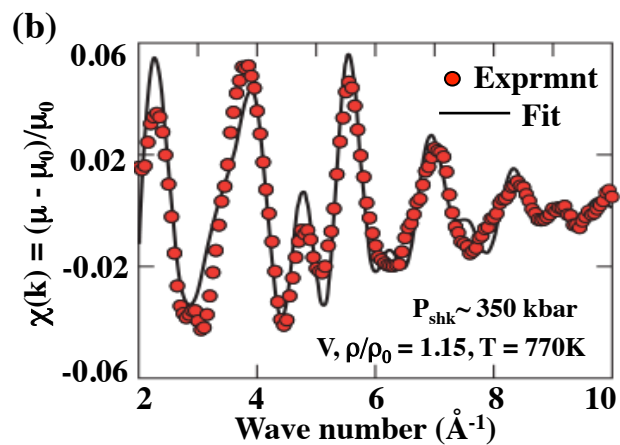
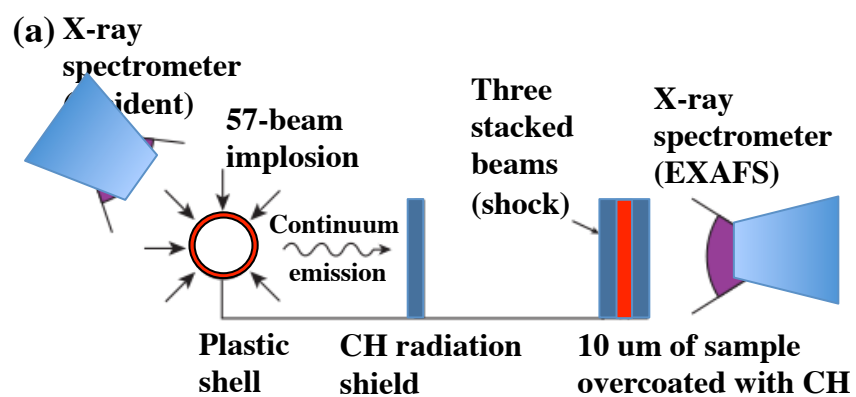


Figure 7

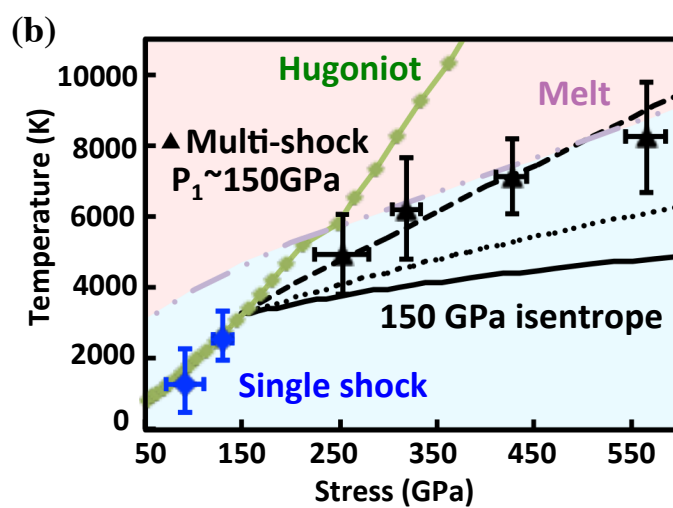
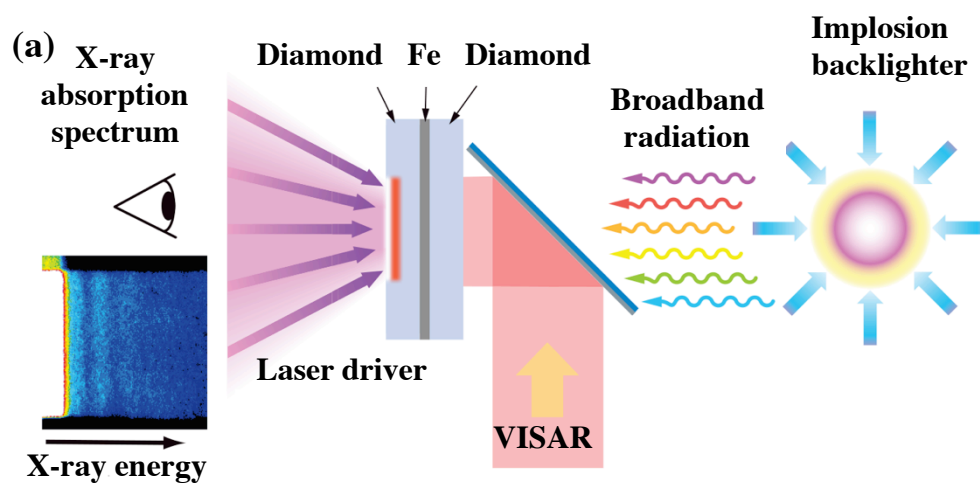


Figure 8

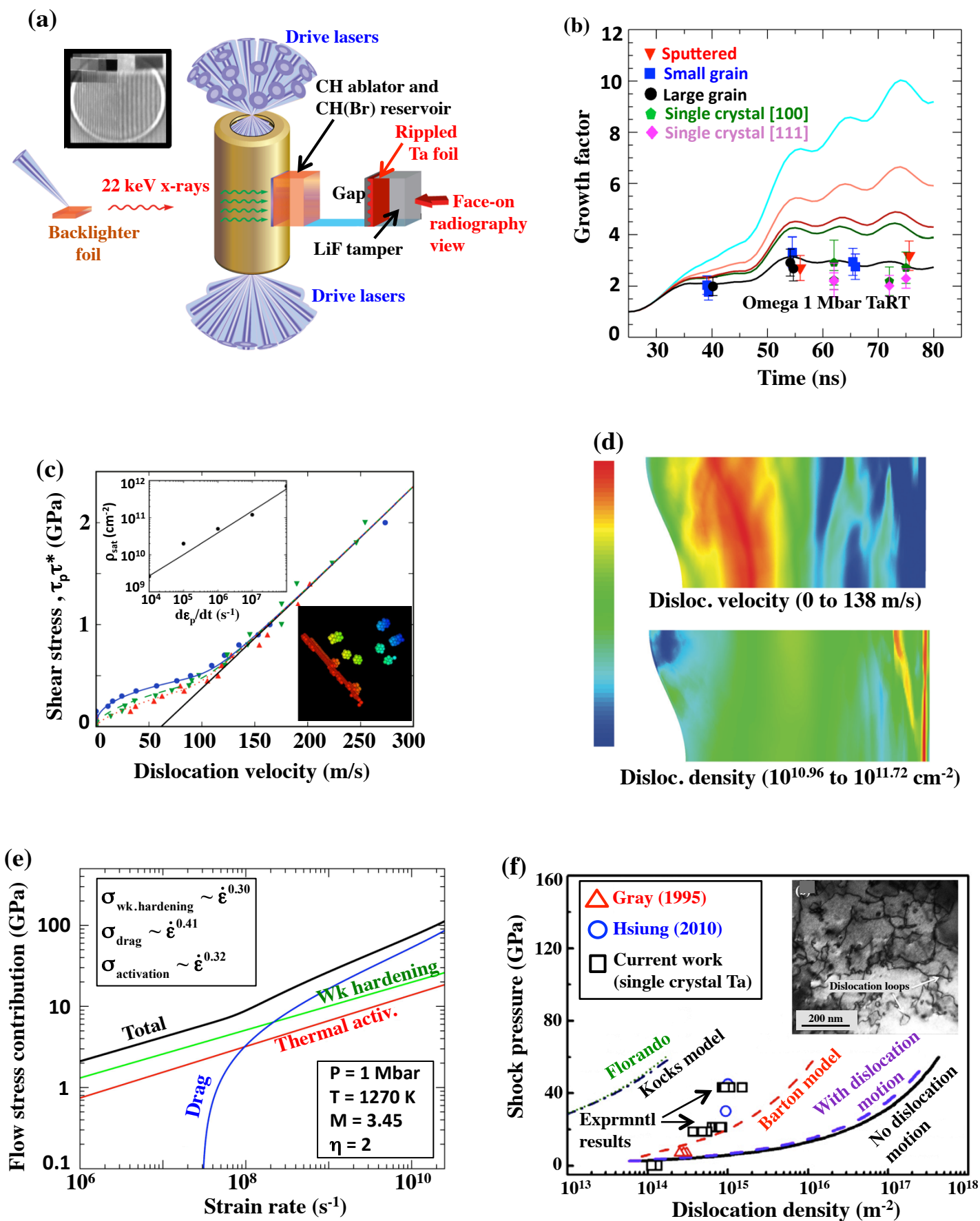


Figure 9

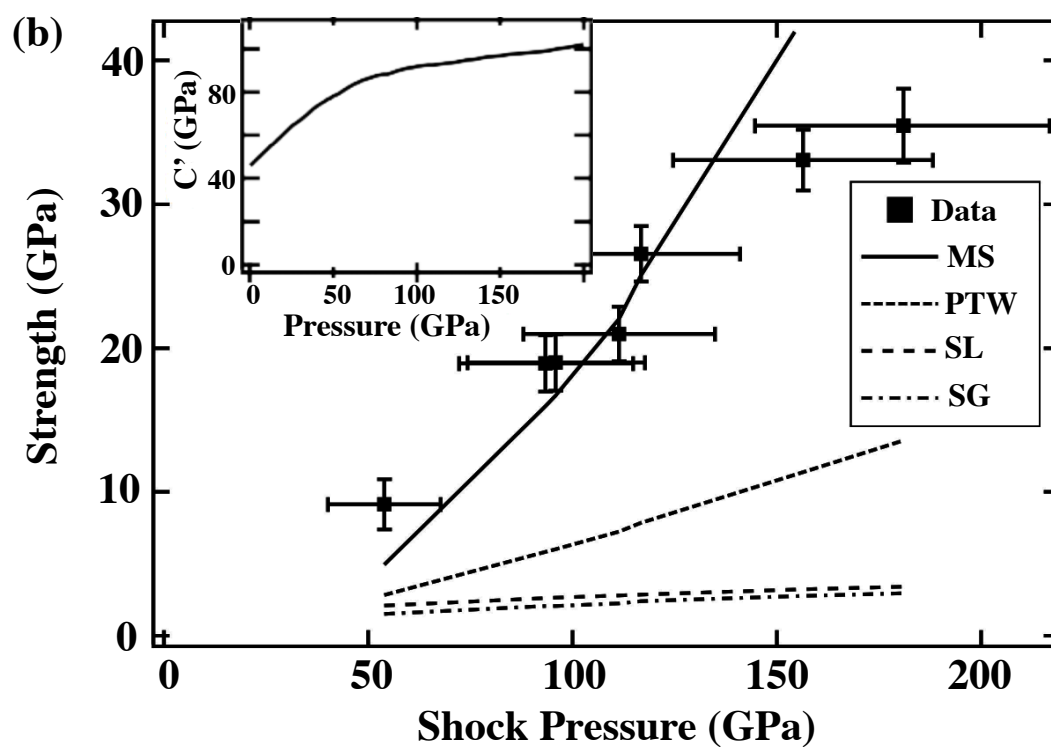
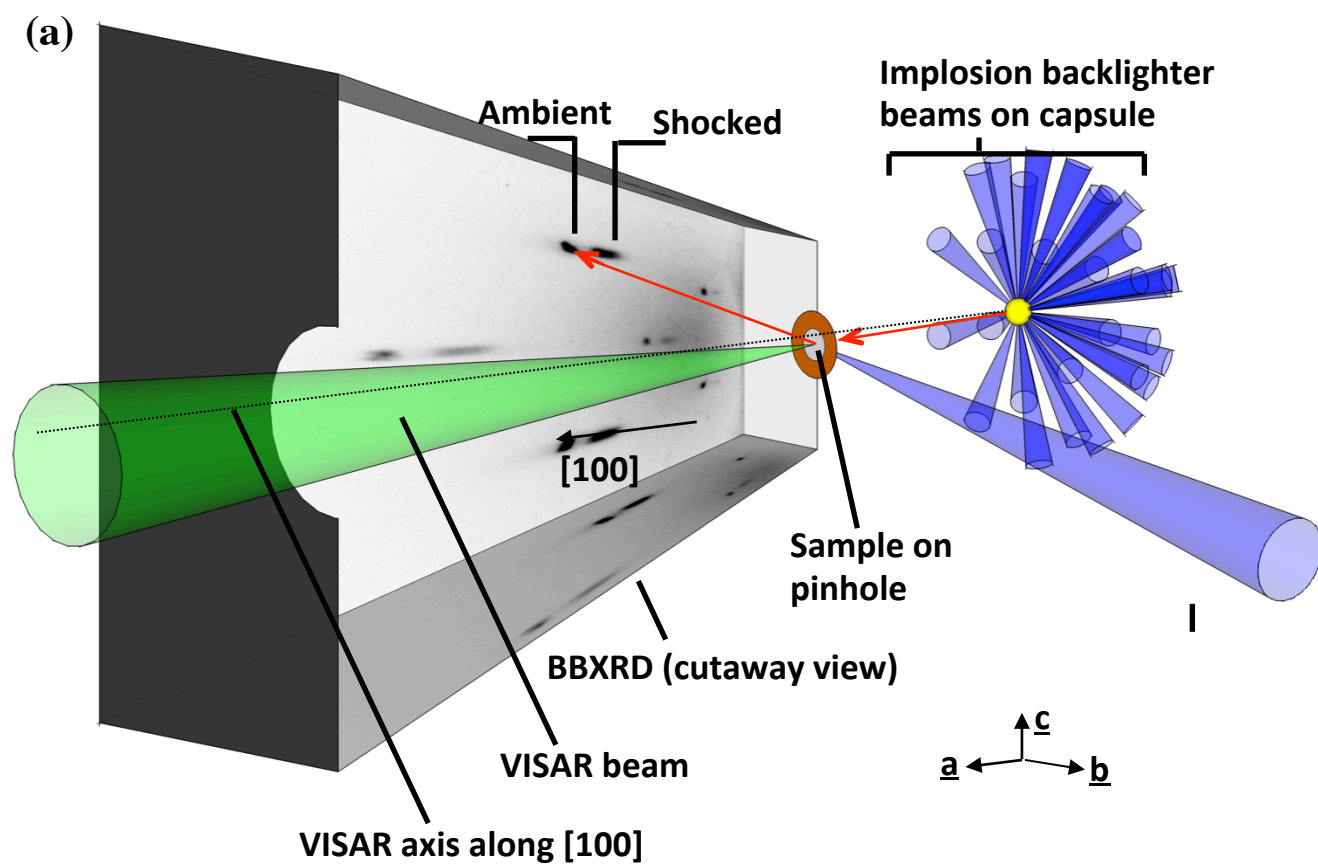


Figure 10

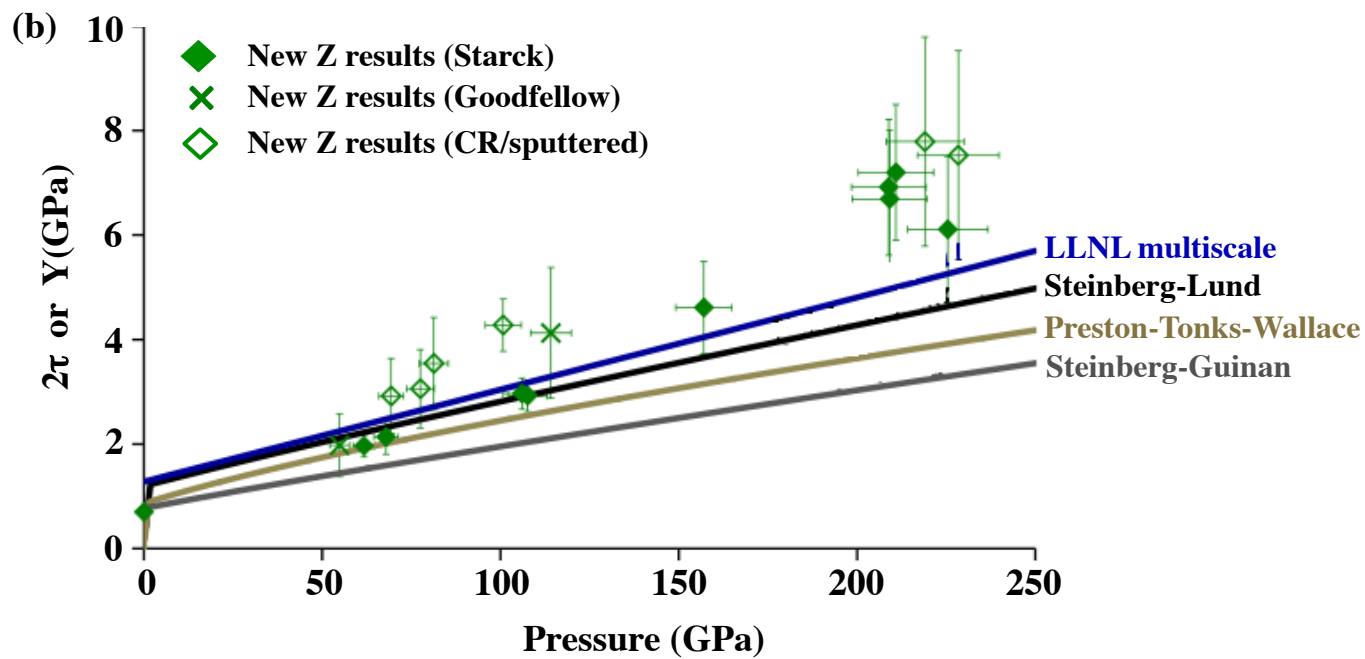
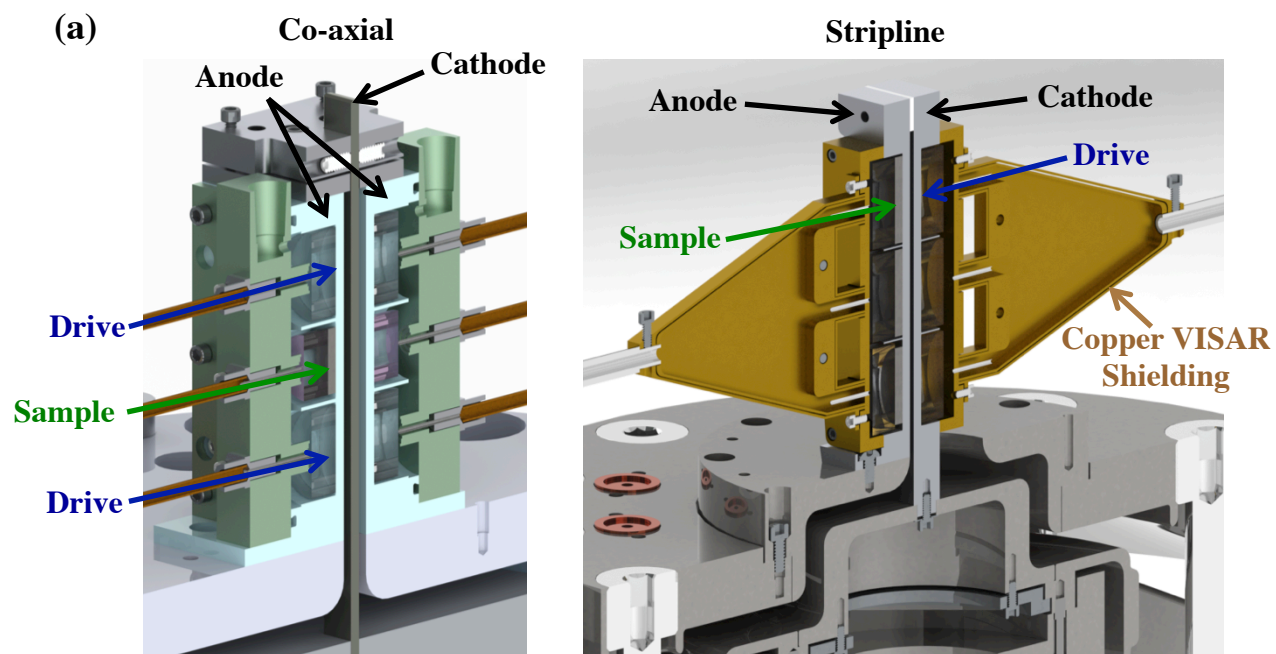


Figure 11

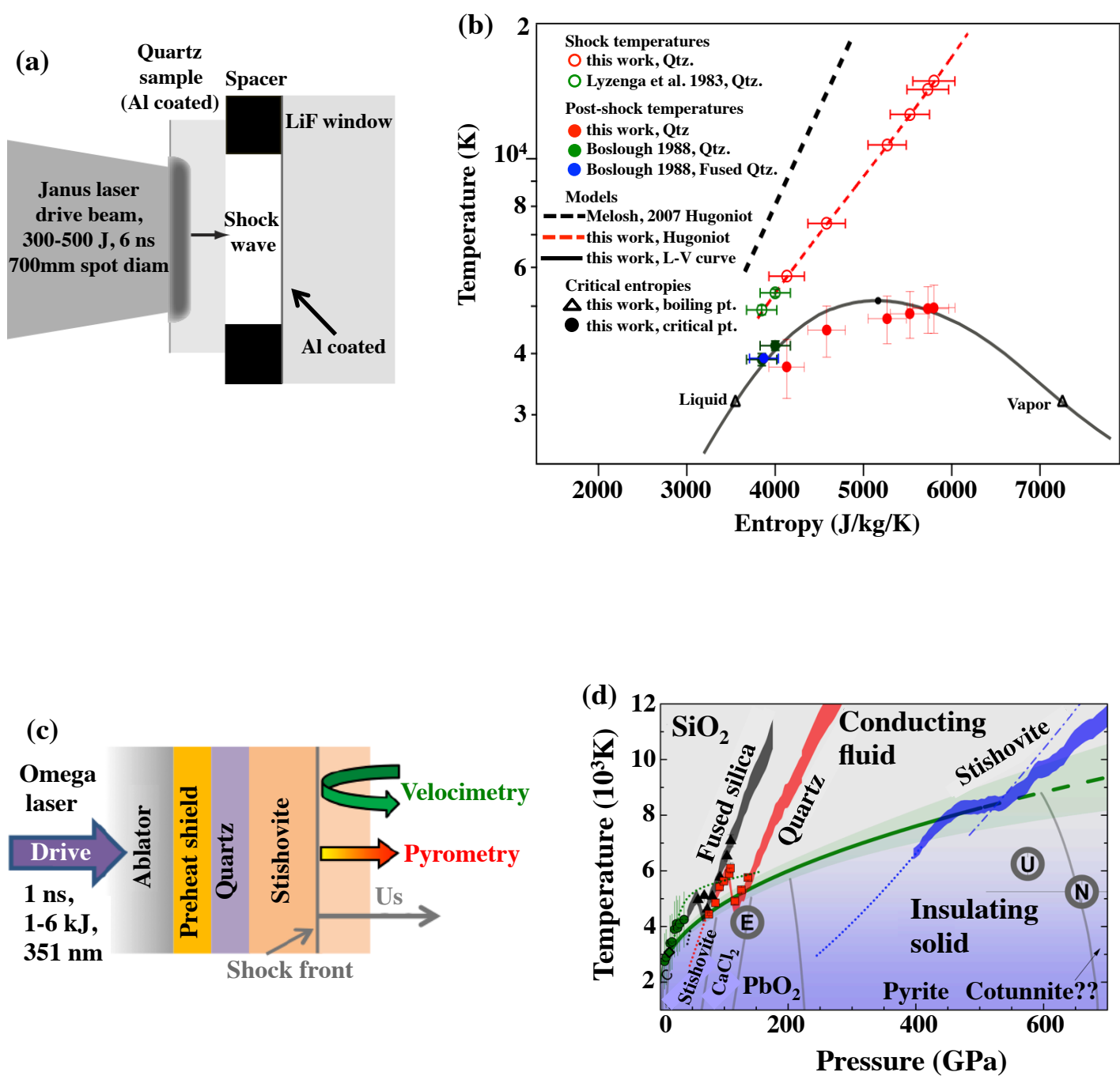


Figure 12

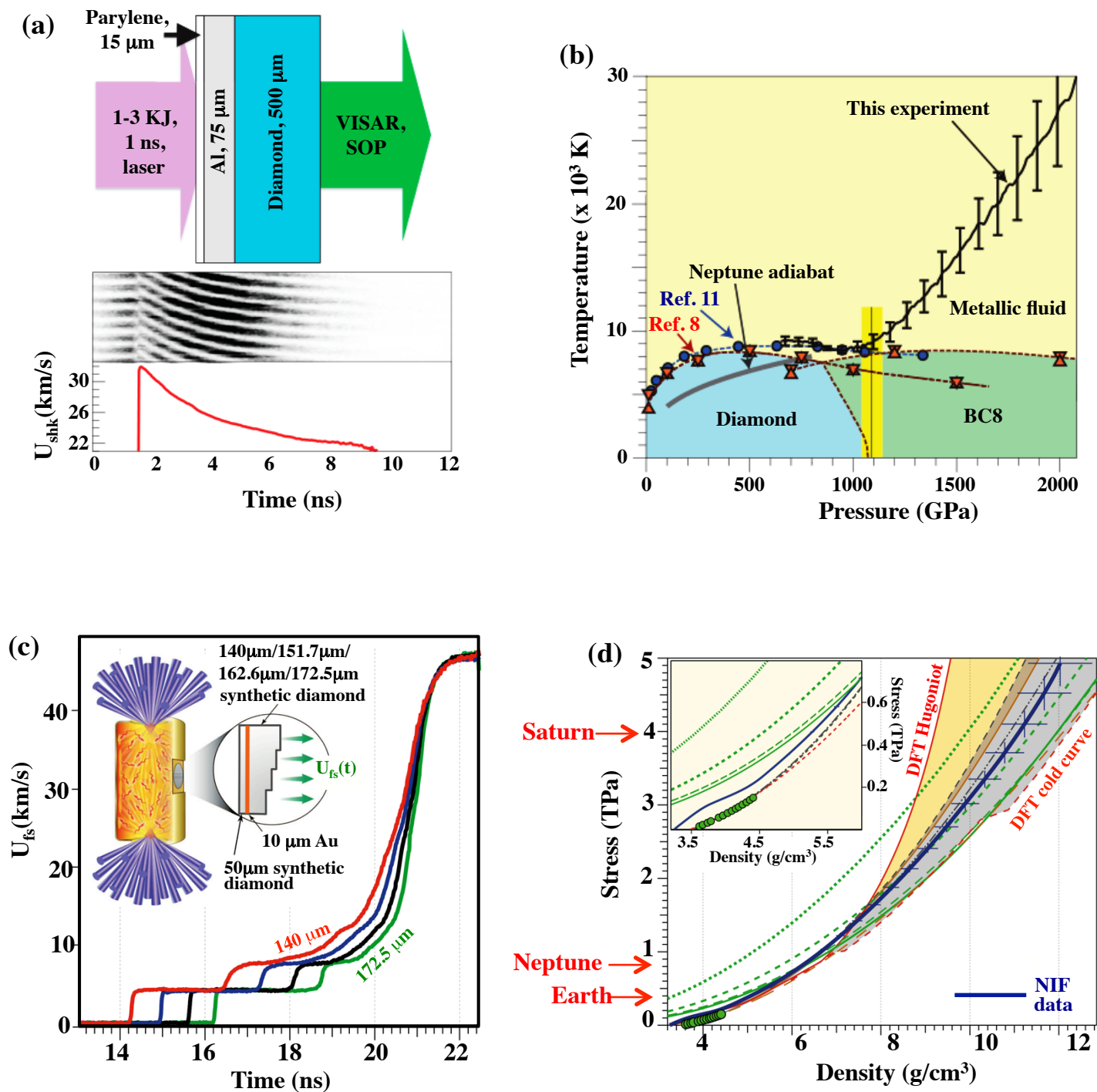


Figure 13

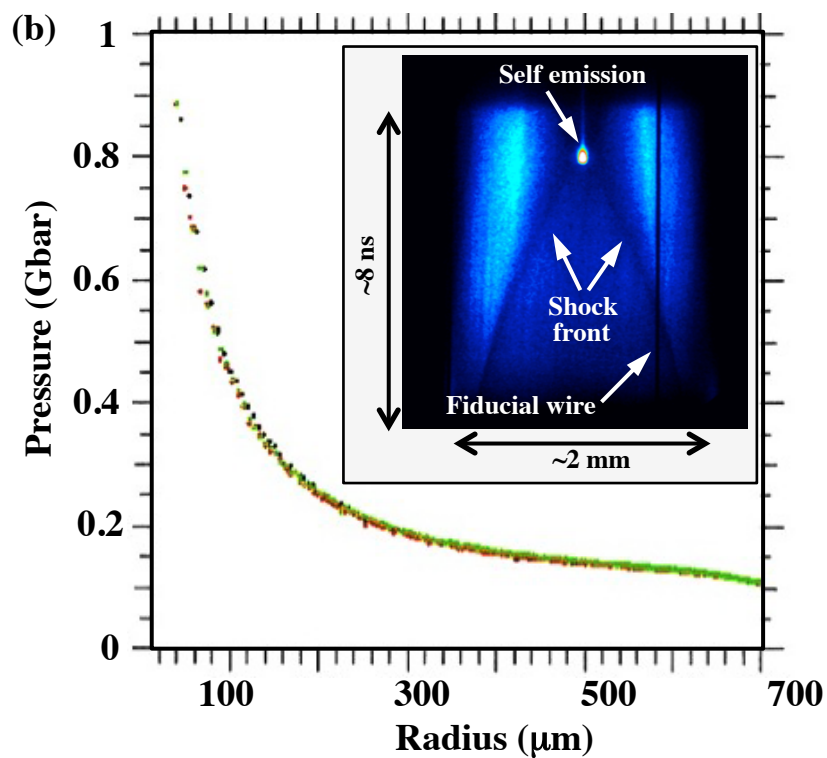
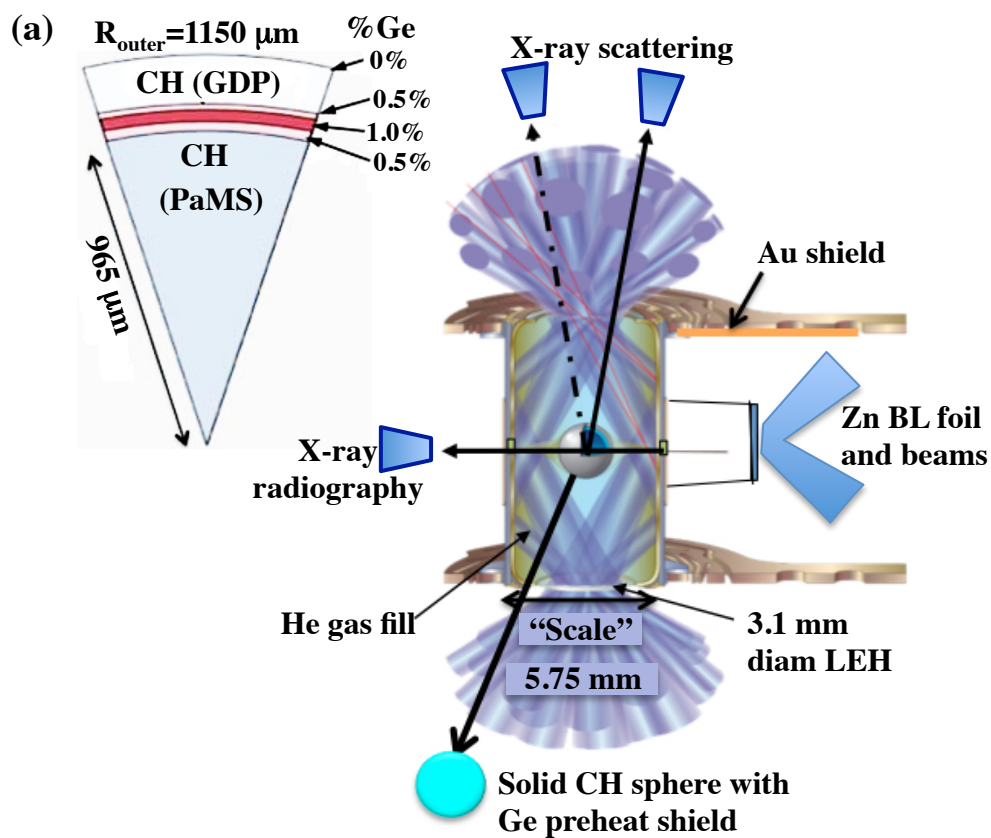


Figure 14

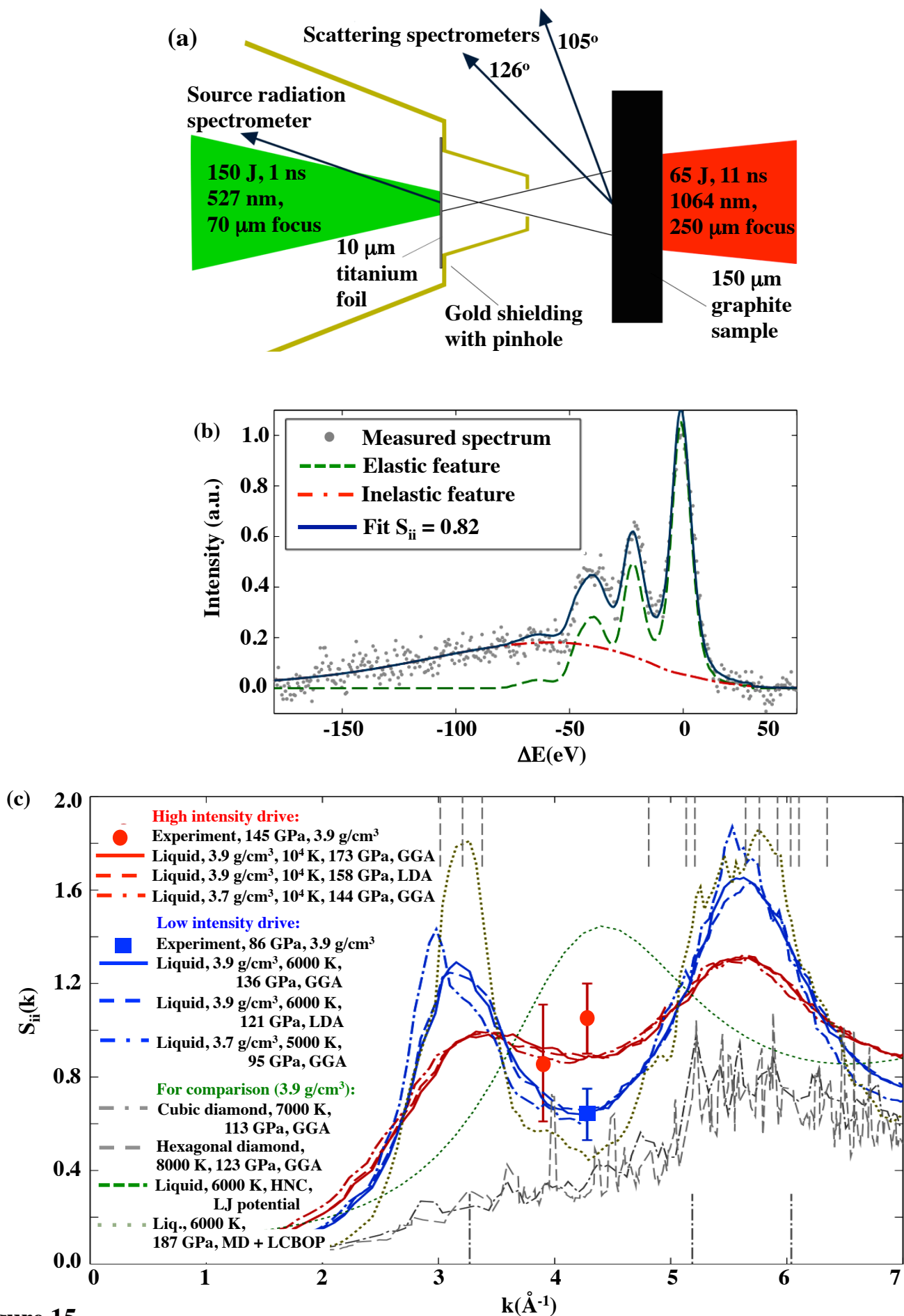


Figure 15